NASA / TP-1999-209369

Solar Cycle Variation and Application to the Space Radiation Environment

John W. Wilson, Myung-Hee Y. Kim, Judy L. Shinn, Hsiang Tai
Langley Research Center, Hampton, Virginia

Francis A. Cucinotta, Gautam D. Badhwar
Johnson Space Center, Houston, Texas

Francis F. Badavi
Christopher Newport University, Newport News, Virginia

William Atwell
Boeing North American, Houston, Texas

September 1999

The NASA STI Program Office . . . in Profile

Since its founding, NASA has been dedicated to the advancement of aeronautics and space science. The NASA Scientific and Technical Information (STI) Program Office plays a key part in helping NASA maintain this important role.

The NASA STI Program Office is operated by Langley Research Center, the lead center for NASA's scientific and technical information. The NASA STI Program Office provides access to the NASA STI Database, the largest collection of aeronautical and space science STI in the world. The Program Office is also NASA's institutional mechanism for disseminating the results of its research and development activities. These results are published by NASA in the NASA STI Report Series, which includes the following report types:

- TECHNICAL PUBLICATION. Reports of completed research or a major significant phase of research that present the results of NASA programs and include extensive data or theoretical analysis. Includes compilations of significant scientific and technical data and information deemed to be of continuing reference value. NASA counterpart or peer-reviewed formal professional papers, but having less stringent limitations on manuscript length and extent of graphic presentations.

- TECHNICAL MEMORANDUM. Scientific and technical findings that are preliminary or of specialized interest, e.g., quick release reports, working papers, and bibliographies that contain minimal annotation. Does not contain extensive analysis.

- CONTRACTOR REPORT. Scientific and technical findings by NASA-sponsored contractors and grantees.

- CONFERENCE PUBLICATION. Collected papers from scientific and technical conferences, symposia, seminars, or other meetings sponsored or co-sponsored by NASA.

- SPECIAL PUBLICATION. Scientific, technical, or historical information from NASA programs, projects, and missions, often concerned with subjects having substantial public interest.

- TECHNICAL TRANSLATION. English-language translations of foreign scientific and technical material pertinent to NASA's mission.

Specialized services that complement the STI Program Office's diverse offerings include creating custom thesauri, building customized databases, organizing and publishing research results . . . even providing videos.

For more information about the NASA STI Program Office, see the following:

- Access the NASA STI Program Home Page at *http://www.sti.nasa.gov*

- Email your question via the Internet to help@sti.nasa.gov

- Fax your question to the NASA STI Help Desk at (301) 621-0134

- Telephone the NASA STI Help Desk at (301) 621-0390

- Write to:
  NASA STI Help Desk
  NASA Center for AeroSpace Information
  7121 Standard Drive
  Hanover, MD 21076-1320

NASA / TP-1999-209369

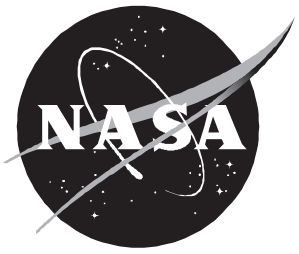

Solar Cycle Variation and Application to the Space Radiation Environment

John W. Wilson, Myung-Hee Y. Kim, Judy L. Shinn, Hsiang Tai
Langley Research Center, Hampton, Virginia

Francis A. Cucinotta, Gautam D. Badhwar
Johnson Space Center, Houston, Texas

Francis F. Badavi
Christopher Newport University, Newport News, Virginia

William Atwell
Boeing North American, Houston, Texas

National Aeronautics and
Space Administration

Langley Research Center
Hampton, Virginia 23681-2199

September 1999

The use of trademarks or names of manufacturers in this report is for accurate reporting and does not constitute an official endorsement, either expressed or implied, of such products or manufacturers by the National Aeronautics and Space Administration.

Available from:

NASA Center for AeroSpace Information (CASI)
7121 Standard Drive
Hanover, MD 21076-1320
(301) 621-0390

National Technical Information Service (NTIS)
5285 Port Royal Road
Springfield, VA 22161-2171
(703) 605-6000

Abstract

The interplanetary plasma and fields are affected by the degree of disturbance that is related to the number and types of sunspots in the solar surface. Sunspot observations were improved with the introduction of the telescope in the seventeenth century, allowing observations which cover many centuries. A single quantity (sunspot number) was defined by Wolf in 1848 that is now known to be well correlated with many space observable quantities and is used herein to represent variations caused in the space radiation environment. The resultant environmental models are intended for future aircraft and space-travel-related exposure estimates.

Introduction

The cyclic variation of the number of sunspots was first observed by Heinrich Schwabe between 1826 and 1843 and led Rudolf Wolf to make systematic observations starting in 1848 (ref. 1). The Wolf sunspot number R is an expression of individual spots and spot groupings, according to the relation $R = k\ (10\ g + f)$ where f is the number of individual sunspots, g is the number of groups, and k is an empirical observational factor depending on site of observation and the individual observer. Apart from the rather arbitrary nature of the Wolf sunspot number definition and the subjective observational factor, the defined quantity has demonstrated success in its correlation to a number of solar observables. Wolf also studied the historical record in an attempt to establish a database on cyclic variations of the past. He established a cycle database to only 1700, although the technology and techniques for careful solar observations were first available in 1610. Gustav Spoerer later suggested a 70-year period before 1716 in which sunspots were rarely observed as the reason for Wolf's inability to extend the cycles into the seventeenth century. Maunder would later suggest a period over which the Sun had changed modality from a period in which sunspots all but disappeared from the solar surface, followed by the appearance of sunspot cycles starting in 1700. Careful studies revealed the problem not to be a lack of observational data but included references to negative observations (refs. 1 and 2). Adding to this understanding of the absence of solar activity cycles were observations of aurorae, which were also absent at the same time. Even the lack of a solar corona during lunar eclipses was noted prior to 1715 (refs. 1 and 3). Excellent reviews of the solar cycle are given by Eddy (ref. 1) and Withbroe (ref. 3).

Modern evidence of a prolonged period of cessation of solar activity in the seventeenth century comes from historical levels of the cosmogenic ^{14}C observed in tree rings (ref. 4) and provides an even older record on solar activity, as the rate of production is controlled (through the modulation of galactic cosmic rays), in part, by solar activity (refs. 1 and 3). The ^{14}C levels also depend on the geomagnetic field strength and the solar particle event fluence, as well as on the dynamics of climate, and especially the ocean's solubility for ^{14}C. One can conclude that the ^{14}C levels are consistent with a minimum of solar cycle activity in the latter half of the seventeenth century and that there are also indications of extended periods of even higher levels of solar activity in the past (refs. 1 and 3). Further evidence indicates that known climatic variations also correlate well with the presence or absence of solar activity cycles (ref. 3). Clearly, the apparent modern cyclic variation of the solar sunspot number is, at best, a temporary phenomenon.

A modern understanding of sunspots starts with G. E. Hale (ref. 5), in which magnetic fields and sunspots are linked. Hale suggested that the sunspot cycle period is 22 years, covering two polar reversals of the solar magnetic dipole field. Babcock (ref. 6) later proposed a qualitative model for the dynamics of the solar outer layers as follows: The start of the 22-year cycle begins with a

well-established dipole field component aligned along the solar rotational axis (fig. 1(a)). The field lines tend to be held by the highly conductive solar plasma of the solar surface. The solar surface plasma rotation rate is different at different latitudes, and the rotation rate is 20 percent faster at the equator than at the poles (one rotation every 27 days). Consequently, the magnetic field lines are wrapped by 20 percent every 27 days. After many rotations, the field lines become highly twisted and bundled, increasing their intensity, and the resulting buoyancy lifts the bundle to the solar surface, forming a bipolar field that appears as two spots, as displayed by the kinks in the field lines in figure 1(b). The sunspots result from the strong local magnetic fields in the solar surface that exclude the light-emitting solar plasma and appear as darkened spots on the solar surface (fig. 2). The leading spot of the bipolar field has the same polarity as the solar hemisphere (fig. 1(b)), and the trailing spot is of opposite polarity (ref. 3). The leading spot of the bipolar field tends to migrate towards the equator, while the trailing spot of opposite polarity migrates towards the solar pole of the respective hemisphere with a resultant reduction of the solar dipole moment. This process of sunspot formation and migration continues until the solar dipole field reverses (after about 11 years). The magnetic field of the spot at the equator sometimes weakens, allowing an influx of coronal plasma that increases the internal pressure and forms a magnetic bubble which may burst and produce an ejection of coronal mass, leaving a coronal hole with open field lines (ref. 3). Such a coronal mass ejection is seen at the top of figure 3. Such holes are a source of the high-speed solar wind. The fluctuations in the bundled fields convert magnetic field energy into plasma heating, producing emission of electromagnetic radiation as intense ultraviolet (UV) and X-rays (ref. 3). The solar dipole field, through similar processes, reverses again at the end of the 22-year cycle.

The sunspot cycle affects the near Earth environment. The ability to project those effects into the future depends on the ability to project the sunspot cycle to future dates and to establish correlations with near Earth environmental quantities. So far, the ability to make such projections has been less than successful. As noted by Withbroe (ref. 3), the 38 different predictions of maximum sunspot number for cycle 21 covered the range of 30 to 203, for which one prediction was bound to agree with observation.

Not all historic sunspot data are of the same quality. It is generally agreed that a consistent set of data has been derived since Wolf's initiation of sunspot surveillance in 1848 (solar cycle 9 to the present). Acceptable values are the observations between 1818 and 1847 (solar cycles 6 to 8), which include the observations of Schwabe (as discussed in ref. 1). The quality diminishes before 1818 to the earliest compilation of Wolf to 1700 (including solar cycles 1 to 5 and earlier cycles which have not been numbered). Most cycle projections are based only on the numbered cycles (1755 to the present) or only on those cycles following 1848 (solar cycle 9 to the present). Alternative prediction schemes have been based on precursor models or statistical models. In the present report, we develop a statistical model based on the accumulating cycle sunspot data to estimate future levels of cycle activity. After the development of the cycle statistical model, we examine the coupling of the solar cycle model to space-related quantities of interest to radiation protection.

Solar Cycle Statistical Model

Given the long history of failures in solar cycle forecasting by even sophisticated methods (ref. 3), it is with some trepidation that we venture into the present study. The main hope for the present model is that errors are self-correcting as cycle observations become available, and the assumption of extrapolation from cycle to cycle is uncertain due to randomizing processes at the close of each cycle. This randomization seems to be in the nature of past cycle variations, as will be shown in the present analysis. Of course, this randomization at the close of each cycle will be a future obstacle in forecasting, unless a fundamental understanding of the transition from cycle to cycle is developed.

The monthly averaged sunspot number is shown in figure 4 for the years 1750 through September 1996 (near minimum at the end of cycle 22). As one can see, the cycle has many maxima and minima within each cycle, and the "solar minimum" and the "solar maximum" are derived by long-term averaging of the monthly sunspot numbers. The estimated dates for solar maxima and minima are given in table 1, including those of the National Oceanic and Atmospheric Administration (NOAA) Space Environmental Center. Cycle 1 is the first full cycle in the figure. The odd cycles have the solar dipole moment aligned along the rotational axis, while even cycles are reversed. There is no immediately obvious pattern in figure 4 other than a general cyclic variation of the 10- to 13-year period, fluctuating amplitude, differing minima, and variable shape. One could imagine that cycles 1 to 4 have similarity to cycles 17 to 20, but the pattern is broken with the dissimilarity of cycles 5 and 6, in comparison with cycles 21 and 22.

In deriving a statistical model for solar cycle projection, we consider the possibility that the statistical populations depend on the orientation of the solar dipole moment. The distribution of the annual averaged maxima of the even, odd, and all cycles is shown in figure 5. The distributions are similar, with a slight shift of even cycles to smaller sunspot maxima. Greater differences between odd and even cycles are seen in the annual averaged minima at the start of each cycle, as shown in figure 6. In this case, odd cycles tend to shift to smaller minima. The cycle duration is nearly independent of the odd-even population, as shown in figure 7. The sunspot minimum is correlated with the cycle maximum, as seen in figure 8, although the scatter about the correlation line is somewhat large. The sunspot number randomizes through the remainder of the cycle so that the succeeding solar minimum is not correlated with the prior cycle maximum, as seen in figure 9. This tendency to randomize at the end of the cycle also indicates the statistical independence of the odd and even cycle populations.

In developing the present model, we assume a difference between even and odd cycles and treat them as two independent populations. Given the time of the prior solar minimum in the current cycle 23, this time is estimated to be September 1996; we generate for each successive month an appropriate (according to even or odd cycle) population distribution and the associated cumulative frequency spectrum. In this way, we calculate the percentile groups for each month after the cycle 23 minimum and display those distributions through 2010 in figure 10. Data from the first nine months of cycle 23 are also shown in figure 10, as the filled circles, and are shown in expanded view in figure 11. The current cycle is running above the 70-percentile group, as seen in the figures. These results depend on the assumed solar minimum, which is not precisely known until well into cycle 23, as the minimum is dependent on the long-term running average of the sunspot number, which cannot be determined except in retrospect.

These results are used to project sunspot number into the future as follows: The current cycle sunspot number at each month is used to calculate the range of percentile groups that contain the current cycle data. This calculation is illustrated in figure 12, where projections for the present solar cycle 23 are based on an assumed minimum in September 1996 (note: the minima and maxima are located on the basis of long-term running averages). The mean percentile grouping of the current cycle is 82 percent, with a standard deviation of 18 percent. Long-term projections based on the results of figure 12 are shown in figure 13. In figure 13, we show the continuation, through part of cycle 24, of the percentile groups for both monthly values and annual average sunspot numbers through 2010. One should bear in mind that randomization will occur near the end of cycle 23, and the appropriate percentile grouping for cycle 24 is independent of cycle 23 variations. Only an improved understanding of how the transition from one cycle to the next is made will allow extrapolation with confidence across cycle boundaries. Note that projections over more than one cycle introduce uncertainties not only in the future amplitude, due to randomization near the cycle boundary, but also reflect uncertainty in the cycle duration. Hence, the estimate of the next solar maximum and minimum is uncertain, in addition to the corresponding

sunspot numbers. As cycle 23 progresses, we may continue to plot the monthly average sunspot numbers and estimates of the percentile group of the expanding cycle 23 observations. The beginning of this process is shown in figure 13. Recall that only the first 9 months of data were used in making the projection, so that the next 12 months of data shown in the figure are a test of the goodness of the projection. It appears that the current cycle will run its course in the high side of the uncertainty band and promises to be one of the larger cycles yet observed. As the cycle progresses, the uncertainty in percentile grouping could be contracted about the expanding current data through reanalysis of the current cycle percentile group (similar to fig. 12) to better define future values within the remainder of the cycle. Adjustment of the cycle 23 minimum may also be dictated by new data.

Because the time to achieve solar maximum is correlated to the percentile group, we may estimate the time to the next solar maximum, as shown in figure 14. Hence, the next solar maximum is currently projected to be in June 2000, with an uncertainty factor of 15 months. The corresponding annual averaged-maximum sunspot number is expected to be 155, with an uncertainty of 26. The duration of cycle 23 is similarly analyzed in figure 15, and the next solar minimum is expected to be in March 2007, with 16 months' uncertainty. The sunspot minimum in March 2007 is expected to be 11, with an uncertainty of 3. The estimates of the cycle 23 maximum and the cycle 24 minimum values are given in table 2.

Radio Flux Output

The energetic UV is important to atmospheric heating that results in an expansion of the atmosphere to higher altitudes. Particles trapped in the Earth's magnetic field at low altitudes impact the atmospheric constituents, losing energy in the collision. The lifetimes of specific energy groups are partly governed by this energy loss (especially at the altitudes below L of 1.25, a region of importance to low Earth orbit operations) (refs. 7 to 9). The symbol *L* is the geomagnetic coordinate equal to the radial distance in Earth radii on the equator. Thus, the expansion of the Earth's atmosphere is important to understanding the trapped radiation levels in low Earth orbit. The UV and X-ray outputs are correlated with the 10.7-cm radio flux output F10.7. Radio output is then an important parameter relating to the trapped radiations in low Earth orbit. The correlation of the 10.7-cm radio flux output, with sunspot number, is shown in figure 16. This correlation does not depend strongly on the cycle number. Because the trapped particles have lifetimes of many days to years, we will use the annual average radio output as one indicator of environmental levels. While it is true that the inner zone radiations are mainly the result of decaying albedo neutrons produced by cosmic rays in the atmosphere, which are correlated with neutron monitor count rate (see next section), the particles are likewise affected by the interaction with the atmosphere that determines their lifetimes. The atmospheric density is related to the radio output.

Galactic Cosmic Ray Modulation

Cosmic rays entering the solar system interact with the outward propagating solar wind, in which is embedded the solar magnetic field. A solution of the Fokker-Planck equation was found by Parker (ref. 10), in which the inward diffusion of galactic cosmic rays is balanced by the outward convection by the solar wind. The density of cosmic ions within the solar system, assuming spherical symmetry, is then related to the external density as

$$\mu(r,R) = \mu_0(R) \exp\left[-\int_r V(r')dr'/\mathrm{D}(r',R)\right] \tag{1}$$

where $\mu(r,R)$ is the ion density at radial distance r and rigidity R (particle momentum per unit charge), $\mu_0(R)$ is the density in interstellar space, $V(r)$ is the solar wind velocity, and $D(r,R)$ is the diffusion coefficient (ref. 11). The wind velocity and diffusion coefficient depend on the solar activity, and there is a phase shift between sunspot number and modulation, as the wind generated at the solar surface diffuses into the modulation cavity that extends far out into the solar system. A simplified version of the diffusion model was implemented by Badhwar and O'Neill (ref. 12), in which the solar wind is held constant at 400 km/sec, and the diffusion coefficient is taken as a function of time and is correlated with the Mount Washington neutron monitor count rate. The diffusion was bimodal, with unique dependence on the orientation of the solar magnetic dipole. Parker assumes an isotropic diffusion coefficient in which the diffusion coefficient generally increases with radial distance as $D(r,R) = D_0(R)r^s$ where s (the exponent for the radial dependance of the diffusion coefficient) is found to be on the order of 0 to 2. The above assumptions lead to

$$\mu(r,R) = \mu_0(R) \exp\left\{-V_0\left(r_0^{1-s} - r^{1-s}\right)/[(1-s)D_0(R)]\right\} \tag{2}$$

where V_0, r_0, and $D_0(R)$ are the wind speed, size of the modulation cavity (50 to 100 AU), and diffusion coefficient at 1 AU, respectively. Equation (2) is used to scale the modulated flux at 1 AU to arbitrary distance. Modulation studies using various Pioneer, Voyager, and Interplanetary Monitoring Platform (IMP) spacecraft show variability of s with the solar cycle for some restricted energy ranges, but the gross behavior for all energies above 70 MeV is well represented by $s = 0.5$ (ref. 13), which we assume hereafter.

The neutrons generated by galactic cosmic rays at the Deep River neutron monitor site (longitude 45° N, latitude 77° W, 145-m altitude) during cycles 19 and 21 are shown in figure 17 as a function of sunspot number. The time delay between changes in the number of sunspots and modulation of the cosmic ray intensities is clearly apparent as a hysteresis in the correlation. There appears to be a reasonably well-established pattern of count rate and sunspot number for these cycles in spite of the much higher sunspot numbers of cycle 19. We have attempted to define a correlation function between the sunspot number on the rising side of the cycle and a second correlation function on the declining side of the cycle. The two correlation functions are bridged by three equal yearly steps, starting 1 year before solar maximum. This correlation model is used in all odd cycles for which the solar polar field and rotational axis are aligned.

The Deep River neutron monitor count rates for cycles 20 and 22 are shown in figure 18. The correlation functions on the rising and declining sides of the even cycles are nearly cycle independent, even though cycle 22 was substantially more intense than cycle 20. The transition from the rising correlation function to the declining correlation function is made only 1 year after solar maximum is achieved. The only exception to the correlation functions is during 1971 and 1972, when the decline of sunspot number was halted by an abrupt increase in sunspot number, during which time it seems that the dynamics are a restart of a cycle before continuing the decline in 1973 and 1974. We have not attempted to model such reversals, although such a model could easily be developed. The transition between cycles is made in the year prior to solar minimum.

As a test on the correlation functions, we show in figure 19 the "predicted" Deep River neutron monitor count rates using sunspot numbers in comparison with the measured values. In the figure we have completed cycle 22 using data from Calgary (N51, W114, 1128-m altitude) and a correlation function between Calgary and Deep River, as the Deep River monitor was discontinued in December 1995. With the exception of 1971 and 1972, as discussed above, the ability to project the Deep River neutron monitor count rate from the sunspot numbers appears relatively accurate. Thus, the ability to project sunspot numbers into the future will allow us to project the cosmic ray intensities with reasonable accuracy.

In past statistical models, the mean of a particular subset of the cycles was used as a predictor of the next cycle (ref. 14). The mean sunspot number, with a broad confidence interval, would be used in the present analysis for crossing the cycle boundaries. A comparison of the Deep River neutron monitor count rate based on this predictor method, as applied to even and odd cycles, is shown in figure 20. Clearly, such projections, when no data on the cycle being projected are available, are often poor; better methods for the transition to successive cycles are needed.

In the Badhwar-O'Neill model (ref. 12), the galactic cosmic annual fluence was evaluated for successive solar maxima and minima since the maximum of solar cycle 19 in 1958. They have further evaluated the corresponding dose and dose equivalents for 0- and 5-cm depths in a water target shielded by 1, 3, 10, and 20 g/cm^2 of aluminum by using the ICRP26 quality factor (ref. 15) and the HZETRN code (ref. 16). We have evaluated the annual average Deep River neutron monitor count rate for each minimum or maximum specified in the Badhwar-O'Neill model and use these values to interpolate the Badhwar-O'Neill model to intermediate years. The corresponding dose equivalent rates using the ICRP 60 quality factors (ref. 17) are shown in figures 21 and 22. The model predicts that cycle 23 will provide a rather large maximum wherein reasonably low doses are received over an extended period. On the other hand, cycle 24 exhibits a narrow maximum period over which doses are relatively large. One should bear in mind that the cycle 24 predications in the present model are very uncertain due to the randomization expected at the end of cycle 23.

Modulation of Atmospheric Ionizing Radiation (AIR)

Atmospheric ionizing radiation (AIR) results from the interaction of cosmic rays with the Earth's atmosphere. As the cosmic ray intensities are modulated by the solar activity, so are the atmospheric radiations modulated with time. The AIR model version 0 is the parametric fit to data gathered by the Langley Research Center studies of the radiations at Supersonic Transport (SST) altitudes in the years 1965 to 1971, covering the rise and decline of solar cycle 20. Scaling of the data with respect to geomagnetic cutoff, altitude, and modulation of the Deep River neutron monitor was found to allow mapping of the environment to all locations at all times, resulting in an empirically based model named AIR model Version 0 (ref. 18). The basic data consisted of tissue equivalent ion chamber rates, fast neutron spectrometer, and nuclear emulsion detection of nuclear reaction products in amino acids (gel). The model was based on global surveys with airplanes and balloons. The latitude surveys by balloons and aircraft are shown for the transition maximum and at subsonic aircraft altitudes of 250 g/cm^2 in figure 23. The curves in the figure are our approximation to the data and are given in terms of rigidity R, atmospheric depth x, and Deep River neutron monitor count rate C in units of the maximum (7157) by

$$\phi(x,R,C) = f(R,C)\ \exp\ (-x/\lambda) - F(R,C)\ \exp\ (-x/\Lambda) \tag{3}$$

where

$$f(R,C) = \exp\ (250/\lambda)\phi_s(R,C) \tag{4}$$

$$F(R,C) = (\Lambda/\lambda) f(R,C)\ \exp\ (x_m/\Lambda - x_m/\lambda) \tag{5}$$

and

$$\Lambda = \lambda[1 - \phi_m(R,C)\ \exp\ (x_m/\lambda)/f(R,C)] \tag{6}$$

$$x_m = 50 + \ln\{2000 + \exp[-2(C - 100)]\} \tag{7}$$

$$\begin{aligned}\phi_s(R,C) = {} & 0.17 + [0.787 + 0.035(\mathrm{C} - 100)] \exp(-R^2/25) \\ & + \{-0.107 - 0.0265(\mathrm{C} - 100) + 0.612 \exp[(\mathrm{C} - 100)/3.73]\} \exp(-R^2/139.2)\end{aligned} \tag{8}$$

$$\begin{aligned}\phi_m(R,C) = {} & 0.23 + [1.1 + 0.0167(\mathrm{C} - 100)] \exp(-R^2/81) \\ & + \{0.991 + 0.051(\mathrm{C} - 100) + 0.4 \exp[(\mathrm{C} - 100)/3.73]\} \exp(-R^2/12.96)\end{aligned} \tag{9}$$

$$\lambda = 160 + 2R \tag{10}$$

The neutron environment model is shown in figure 23 in comparison to experimental measurements. The flux from 1 to 10 MeV is converted to dose equivalent and dose rates by using 3.14 μSv-(cm^2/s)/hr and 0.5 μGy-(cm^2/s)/hr, respectively. These coefficients are based on older dosimetric relations, as described by Foelsche et al. (ref. 19). The current estimates use the ICRP 60 quality factor (ref. 17), which increases the neutron dose equivalent by about 55 percent, relative to the ICRP26 values.

Unfortunately, not all ion chamber data or all nuclear emulsion data were reduced. For our purpose, we use argon-filled ion chamber data to represent the altitude, latitude, and solar cycle dependence of dose from all components except neutrons, and we use the available tissue equivalent ion chamber data as a guide. The argon-filled ion chamber data of Neher and Anderson (refs. 20 and 21) was compiled by Curtis et al. (as mentioned in ref. 22) at the 1965 solar minimum ($C = 98.3$) in table 3 and the 1958 solar maximum ($C = 80$) in table 4. We have augmented the table by Curtis with data from the work of Neher and Anderson. Note that the low-energy GCR had not fully recovered in the summer of 1965, with the result that the high-latitude ionization at high altitude is about 10 percent lower than that in 1954. Furthermore, the 1958 measurements near solar maximum covered only at mid-to-high latitudes, and the low-latitude data in table 4 are likely to be about 10 percent too high at high altitudes. The ionization rates in tables 3 and 4 are the rates in air per atmosphere of pressure (directly related to the exposure unit Roentgen). The atmospheric ionization rates are interpolated in altitude, geomagnetic cutoff, and solar modulation and are directly converted to exposure units and absorbed dose in tissue. The comparison with the tissue equivalent ion chamber requires the addition of the neutron-absorbed dose rates, and good consistency between this method and the tissue equivalent ion chamber has been demonstrated (ref. 18). Dose equivalent estimates require an estimate of the high LET components associated with charged particles and are found from the measurements in nuclear emulsion, as shown elsewhere (refs. 18 and 19). The corresponding average quality factor for the argon ion chamber dose is

$$Q = 1 + 0.35 \exp(-x/416) - 0.194 \exp(-x/65) \tag{11}$$

This quality factor is to be applied only to the dose component derived from the argon ion chamber. The approximate average quality factor, given by equation (11), was fit to data at high latitudes and high altitudes and is a source of uncertainty elsewhere in the atmosphere. Note that Q, as given by equation (11), declines to unity deep in the atmosphere where muons dominate the exposure as expected.

In the present version of the model, we use the Deep River neutron monitor data where available, predict the Deep River neutron monitor count rate by using known sunspot numbers when they are available, and project sunspot numbers by assuming the appropriate percentile (82 percent for cycle 23)

for future dates. A conservative projection for a future cycle, for which there are yet no data, should be used in the sense that exposures would not likely be underestimated. This conservatism would use the 10-percentile group for the sunspot number. As cycle sunspot data are obtained, improved projections can be made, as illustrated in the discussion of figure 11. The high-altitude exposures that use the ICRP 60 quality factor in the atmosphere are shown in figure 24 by using the 82 percentile group for projection.

Modulation of Trapped Radiations

The particles trapped in the geomagnetic field were modeled for data obtained during two epochs of solar cycle 20 (the solar minimum of 1964 and the solar maximum of 1970), and best estimates of magnetic field coordinates were taken from current field models at the time of measurement (ref. 23). The 1964 analysis using magnetic field model IGRF-65/epoch 1964 resulted in particle population maps AP8 MIN and AE8 MIN for trapped protons and electrons, respectively. The 1970 analysis using the magnetic field model United States Coast & Geodetic Survey/epoch 1970 resulted in the particle population maps of AP8 MAX and AE8 MAX. It was believed at one time that better estimates of particle environments could be gained by evaluating the population maps defined on invariant McIlwain coordinates over current magnetic field estimates. This interpolation would, for example, contain the westward shift of the south Atlantic anomaly observed in recent years by Badhwar et al. (ref. 24). However, it was recognized by the Shuttle dosimetry group (ref. 23) that large errors resulted from such a procedure, and it was concluded that the use of the particle population maps interpolated over the field model, for which the population map was derived, would provide the best estimates of the long-term, orbital-averaged particle environments, even though the westward shift is not represented. A comparison of the Shuttle dosimetric results at various times in the last few solar cycles and model calculations is shown in figure 25. The upper curve is for solar minimum (1964) and the lower curve for solar maximum (1970). The triangles are interpolations that use the solar 10.7-cm radio output evaluated by Atwell et al. (ref. 23).

Following the work of Atwell et al. (ref. 23), we have used the 10.7-cm radio output to scale the trapped electron environments as a function of solar cycle. The rationale is that the outer zone electrons are trapped through the magnetospheric tail and are lost after radial diffusion into the atmosphere near the polar regions. The injection and the atmospheric loss are correlated with the radio output at 10.7 cm, which is used herein as the appropriate interpolating function. The electron flux is assumed to be

$$f_e(E) = f_{e,\min}(E) \exp\left(-\alpha_e F_{10.7}\right) \tag{12}$$

where $f_{e,\min}(E)$ is the electron flux at solar minimum and α_e is evaluated by using AE8 MAX data derived from cycle 20 measurements. In the model, we use the prior 15-month average of the 10.7-cm radio output for $F_{10.7}$. The proton environment has, as its source, the neutron albedo, and the losses occur through atmospheric interaction. The proton environment is then proportional, in steady state, to the source and the lifetime due to atmospheric interaction (ref. 25). The interpolation procedure is then taken as the product of neutron monitor count rate and solar radio output at 10.7 cm. The proton flux is then extrapolated as

$$f_p(E) = f_{p,\min}(E) \exp\left[-\alpha_p\left(\mathrm{DRNM}\ F_{10.7}\right)\right] \tag{13}$$

where $f_{p,\min}(E)$ is the proton flux at solar minimum, and α_p is evaluated by using the AP8 MAX data derived from cycle 20 measurements. In the model, the quantity $\left(\text{DRNM } F_{10.7}\right)$ is averaged over the prior 15 months.

The electron and proton environment in the International Space Station (ISS) orbit of 51.6° inclination and at an altitude of 400 km is shown in figures 26 and 27. Figure 26 shows the electron flux at three energies (0.5, 1, and 3 MeV), as a function of radio flux (W/m^2-s). The curves are found by interpolation, using a 15-month average of the radio flux data with assumed exponential dependence in equation (12) and hysteresis results from the difference in averaging on the rising and declining side of the cycle. The odd cycles are shown in figure 26(a), and the even cycles are shown in figure 26(b) for the years 1955 to 2005. The outermost curve is for cycle 19, the largest observed cycle. The inner loops of figure 26(a) are cycles 21 and 23. The even cycles, 20 and 22, are shown in figure 26(b). The inner loop is cycle 20, for which the AE8 MIN and MAX database is derived. The extreme right is the AE8 MAX model and the extreme left is the AE8 MIN model. One can see clearly that most cycles require extrapolation far beyond the cycle 20 data set. The proton flux is assumed to depend on the 15-month average of the Deep River neutron monitor count rate and radio flux output with exponential dependence, as given by equation (13). The results are shown in figure 27. The odd cycles are shown in figure 27(a), and even cycles are shown in figure 27(b). The hysteresis now arises from the hysteresis in the Deep River neutron monitor count rate as well as from the averaging over the ascending and descending phase of the cycle. Cycle 19 is the outer most loop in figure 27(a), while cycles 21 and 23 are the inner loops. Cycle 20, for which measurements were made, is the inner loop in figure 27(b), and the outer loop is cycle 22.

The time dependence is shown in figure 28. The electron flux is shown in figure 28(a) at the three energies of 0.5, 1, and 3 MeV. The variation over time is largest for the 0.5-MeV data and reaches significantly higher values for most cycles than does the AE8 MAX of cycle 20. The proton flux variations are greatest for the lowest proton energies but are still significant at the highest energies. Again we notice that much larger variations occur during most cycles, compared to the variation of cycle 20. We emphasize that these results are tentative and will be tested against Shuttle measurements in the near future.

Variations at zero inclinations are shown in figure 29. Although no precise comparison can be made with the data on the geomagnetic equator of Huston, Kuck, and Pfitzer (ref. 26), a qualitative comparison can be made at zero inclination because the equatorial orbits oscillate about the magnetic equator. In figure 29, the odd cycles have a narrower hysteresis loop compared to the even cycles; otherwise, they cover similar dynamic ranges. Compared with the data of Huston, Kuck, and Pfitzer, cycle 22 in the present model (outer loop in fig. 29(b)) covers a smaller dynamic range (about a factor of 4) than the Huston, Kuck, and Pfitzer analysis (about a factor of 10). The loops of the Huston results are nearly a factor of 8 for flux values on the rising cycle, compared with the flux values on the declining cycle at the lowest altitude ($L = 1.14$). The present results are only a factor of 2 to 3. One can also note that the Huston, Kuck, and Pfitzer result at the highest altitude ($L = 1.2$) shows no general decline over the cycle, while the results in figure 29 show a general decline on the order of a factor up to 1.5 from solar minimum to solar maximum.

Concluding Remarks

Even though little success in the past has been achieved in predicting the solar cycle variation, we have developed a statistical model which has shown some promise in the first 21 months of cycle 23 and

can be updated as the cycle progresses, allowing a convergence toward improved estimates as the cycle progresses. There is still a problem in cycle projection from one cycle to the next because a randomization process occurs at the end of each cycle. Only by a dynamic model based on some yet unidentified observable factor will allow reliable predictions of successive cycle dependence. The purpose of the current projection is to provide a basis of estimating exposures in future missions. The uncertainties of such predictions are clearly large, and the effect of these uncertainties on future shield design requires further study.

References

1. Eddy, John A.: The Maunder Minimum. *Science*, vol. 192, no. 4245, June 1976, pp. 1189–1202.
2. Feynman, J.; and Silverman, S.: Variations of the Solar Wind and Solar Cycle in the Last 300 Years. *Study of the Solar Cycle From Space*, NASA CP-2098, 1980.
3. Withbroe, George L.: Solar Activity Cycle: History and Predictions. *J. Spacecr. & Rockets*, vol. 26, no. 6, Nov.–Dec. 1989, pp. 394–402.
4. Seuss, Hans E.: Secular Variations of the Cosmic-Ray-Produced Carbon 14 in the Atmosphere and Their Interpretations. *J. Geophys. Res*., vol. 70, no. 23, Dec. 1965, pp. 5937–5952.
5. Hale, G. E.: Magnetic Field in Sun-Spots. *Astrophys. J*., vol. 28, 1908, pp. 315–343.
6. Babcock, H. W.: The Topology of the Sun's Magnetic Field and the 22-Year Cycle. *Astrophys. J*., vol. 133, no. 2, Mar. 1961, pp. 572–587.
7. Blanchard, R. C.; and Hess, W. N.: *Solar Cycle Effects on Inner Zone Protons*. NASA TN D-3086, 1966.
8. Dragt, A. J.: Solar Cycle Modulation of the Radiation Belt Proton Flux. *J. Geophys. Res*., vol. 76, Apr. 1971, pp. 2313–2344.
9. Vette, James I.: *The NASA/National Space Science Data Center Trapped Radiation Environment Model Program, 1964–1991*. NASA TM-107993, 1991.
10. Parker, E. N.: The Passage of Energetic Charged Particles Through Interplanetary Space. *Planet. & Space Sci*., vol. 13, Jan. 1965, pp. 9–49.
11. Balasubrahmanyan, V. K.; Boldt, E.; and Palmeira, R. A. R.: Solar Modulation of Galactic Cosmic Rays. *J. Geophys. Res*., vol. 72, Jan. 1967, pp. 27–36.
12. Badhwar, G. D.; and O'Neill, P. M.: Improved Model of Galactic Cosmic Radiation for Space Exploration Missions. *Nucl. Tracks & Rad. Meas.*, vol. 20, no. 3, July 1992, pp. 403–410.
13. Fujii, Z.; and McDonald, F. B.: Radial Intensity Gradients of Galactic Cosmic Rays (1972–1995). *J. Geophys. Res*., vol. 102, no. A11, 1997, pp. 24201–24208.
14. Sleeper, H. P., Jr.: *Planetary Resonances, Bi-Stable Oscillation Modes, and Solar Activity Cycles*. NASA CR-2035, 1972.
15. Badhwar, Gautam D.; Cucinotta, Francis A.; and O'Neill, Patrick M.: An Analysis of Interplanetary Space Radiation Exposure for Various Solar Cycles. *Radiat. Res.*, vol. 138, no. 2, 1994, pp. 201–208.
16. Wilson, John W.; Badavi, Francis F.; Cucinotta, Francis A.; Shinn, Judy L.; Badhwar, Gautam D.; Silberberg, R.; Tsao, C. H.; Townsend, Lawrence W.; and Tripathi, Ram K.: *HZETRN: Description of a Free-Space Ion and Nucleon Transport and Shielding Computer Program*. NASA TP-3495, 1995.
17. International Commission on Radiological Protection: *Radiation Protection: 1990 Recommendations of the International Commission on Radiological Protection.* ICRP Publ. 60, 1992.
18. Wilson, John W.; Townsend, Lawrence W.; Schimmerling, Walter S.; Khandelwal, Govind S.; Khan, Ferdous S.; Nealy, John E.; Cucinotta, Francis A.; Simonsen, Lisa C.; Shinn, Judy L.; and Norbury, John W.: *Transport Methods and Interactions for Space Radiations*. NASA RP-1257, 1991.

19. Foelsche, T.; Mendell, R. B.; Wilson, J. W.; and Adams, R. R.: *Measured and Calculated Neutron Spectra and Dose Equivalent Rates at High Altitudes—Relevance to SST Operations and Space Research.* NASA TN D-7715, 1974.

20. Neher, H. V.: Cosmic-Ray Knee in 1958. *J. Geophys. Res*., vol. 66, no. 12, Dec. 1961, pp. 4007–4012.

21. Neher, H. V.; and Anderson, Hugh R.: Cosmic Rays at Balloon Altitudes and the Solar Cycle. *J. Geophys. Res*., vol. 67, no. 4, Apr. 1962, pp. 1309–1315.

22. The Boeing Co.: *Computation of Galactic Cosmic Radiation Exposure During Aircraft Flights*. Seattle, WA: Document No. DGA 11471-1, 1969.

23. Atwell, William; Beever, E. R.; Hardy, A. C.; Richmond, R. G.; and Cash, B. L.: Space Radiation Shielding Analysis and Dosimetry for the Space Shuttle Program. *High-Energy Radiation Background in Space*, A. C. Rester, Jr., and J. I. Trombka, eds., AIP Conference Proceedings No. 186, 1989, pp. 289–296.

24. Badhwar, G. D.; Golightly, M. J.; Konradi, A.; Atwell, W.; Kern, J. W.; Cash, B.; Benton, E. V.; Frank, A. L.; Sanner, D.; Keegan, R. P.; Frigo, L. A.; Petrov, V. M.; Tchernykh, I. V.; Akatov, Uy A.; Shurshakov, V. A.; Arkhangelsky, V. V.; Kushin, V. V.; Klyachin, N. A.; Vana, N.; and Schoner, W.: In-Flight Radiation Measurements on STS-60. *Radiat. Meas*., vol. 26, no. 1, 1996, pp. 17–34.

25. Blanchard, R. C.; and Hess, W. N.: *Solar Cycle Changes in Inner Zone Protons*. NASA TM-X-55013, 1964.

26. Huston, S. L.; Kuck, G. A.; and Pfitzer, K. A.: Solar Cycle Variation of the Low-Altitude Trapped Proton Flux. *Adv. Space Res.*, vol. 21, no. 12, pp. 1625–1634.

Table 1. Sunspot Maxima and Minima for Cycles 1–22

[NOAA is National Oceanic and Atmospheric Administration.]

Solar cycle	Solar minimum		Solar maximum	
	NOAA	Running average[a]	NOAA[b]	Running average[a]
1	1755.2	1755(7)	1761.5	1761(5)
2	1766.5	1766(2)	1769.7	1769(11)
3	1775.5	1775(7)	1778.4	1778(8)
4	1784.7	1784(5)	1788.1	1788(2)
5	1798.3	1798(4)	1804(1805.2)	1804(8)
6	1810.6	1810(8)	1816.4	1816(7)
7	1823.3	1823(1)	1830(1829.9)	1829(11)
8	1833.9	1833(10)	1837.2	1837(4)
9	1843.5	1843(10)	1848.1	1848(5)
10	1856.0	1856(2)	1860.1	1860(2)
11	1867.2	1867(2)	1870.6	1870(10)
12	1878.9	1878(8)	1883.9	1883(11)
13	1889.6	1889(5)	1893(1894.1)	1893(10)
14	1901.7	1901(8)	1905(1907.0)	1906(4)
15	1913.6	1913(2)	1917.6	1917(11)
16	1923.6	1923(5)	1928.4	1928(2)
17	1933.8	1933(8)	1937.4	1937(10)
18	1944.2	1944(2)	1947.5	1948(1)
19	1954.3	1954(2)	1957.9	1958(1)
20	1964.9	1964(10)	1968.9	1969(2)
21	1976.5	1976(2)	1979.9	1980(2)
22	1986.8	1986(2)	1989.6	1989(11)

[a]Values in parentheses denote the month.

[b]Values in parentheses denote uncertainty.

Table 2. Predicted Sunspot Cycle Parameter to End of Cycle 23

Parameters	Statistical prediction		
	Low end of range	Average	High end of range
Date of smoothed cycle maximum	March 1999	June 2000	September 2001
Smoothed sunspot number at maximum	129	155	181
Date of smoothed cycle 24 minimum	November 2005	March 2007	July 2008
Smoothed sunspot number at minimum	9	11	14

Table 3. Ionization Rates in Air Measured by Argon-Filled Chambers[a] at Solar Minimum ($C = 98.3$ in 1965)

[R is cutoff rigidity]

R, GV	Ion pairs, cm^{-3}-sec^{-1}, for air depths, g/cm^2, of—													
	30	40	50	60	70	80	90	100	120	140	200	245	300	1034
0	445.0	430.0	414.0	399.0	383.0	366.0	349.0	332.0	298.0	266.0	181.0	136.0	95.0	11.4
.01	445.0	430.0	414.0	399.0	383.0	366.0	349.0	332.0	298.0	266.0	181.0	136.0	95.0	11.4
.16	444.0	430.0	414.0	399.0	383.0	366.0	349.0	332.0	298.0	266.0	181.0	136.0	95.0	11.4
.49	411.8	404.3	394.4	382.0	369.0	354.8	339.4	325.0	292.3	264.5	181.0	136.0	95.0	11.4
1.97	325.0	333.0	340.0	335.0	330.0	312.5	308.0	300.0	285.0	264.0	181.0	134.0	95.0	11.4
2.56	300.0	305.0	310.0	305.0	300.0	290.0	285.0	280.0	255.0	230.0	173.0	126.0	95.0	11.4
5.17	185.0	195.0	208.0	208.0	208.0	208.0	208.0	208.0	195.0	185.0	135.0	103.0	75.0	10.6
8.44	127.6	137.0	145.0	150.2	153.8	155.8	156.0	154.6	149.7	142.2	111.3	87.0	66.6	10.4
11.70	85.0	92.0	98.0	100.0	102.0	105.0	107.0	110.0	108.0	105.0	80.0	77.0	60.0	10.0
14.11	70.0	75.0	82.0	85.0	89.0	93.6	95.0	100.0	98.0	95.0	78.0	68.0	50.0	10.0
17.00	66.3	73.8	80.0	84.8	88.5	91.1	92.6	93.5	93.4	90.5	75.0	62.3	48.0	10.0

[a]Experimental data extrapolated to provide estimates of ionization rates over a wide range of altitudes and geomagnetic cutoffs.

Table 4. Ionization Rate in Air Measured by Argon-Filled Chambers[a] at Solar Minimum ($C = 80$ in 1958)

[R is cutoff rigidity]

R, GV	Ion pairs, cm^{-3}-sec^{-1}, for air depths, g/cm^2, of—													
	30	40	50	60	70	80	90	100	120	140	200	245	300	1034
0	264.6	267.5	267.0	265.0	258.0	252.0	243.0	235.0	216.3	197.0	145.0	109.2	78.8	11.4
.01	264.6	267.8	267.0	265.0	258.0	251.0	243.0	235.0	216.3	197.0	145.0	109.2	78.8	11.4
.16	264.6	264.9	265.0	264.0	257.0	250.0	243.0	233.0	215.0	197.0	145.0	109.2	78.8	11.4
.49	264.0	264.9	265.0	262.0	256.0	249.0	242.0	231.0	213.2	197.0	145.0	109.2	78.8	11.4
1.97	264.0	265.0	265.0	262.0	252.0	245.0	241.0	231.0	212.5	197.0	145.0	107.8	78.8	11.4
2.56	235.0	237.5	240.0	240.0	239.0	238.0	237.0	230.0	209.0	197.0	145.0	101.6	78.8	11.4
5.17	162.5	168.0	179.0	182.0	178.0	175.2	174.0	173.8	170.0	160.0	159.0	88.3	65.0	10.6
8.44	95.0	103.5	112.0	118.0	118.0	119.0	120.0	122.0	118.0	117.0	100.6	78.7	60.2	10.4
11.70	78.2	85.0	90.7	92.7	94.8	98.0	100.0	103.1	101.2	98.4	75.0	72.2	56.2	10.0
14.11	65.7	70.7	77.5	80.5	84.3	89.0	90.5	95.3	93.5	90.9	74.0	65.9	47.9	10.0
17.00	63.0	70.3	76.4	81.1	84.8	87.5	89.1	90.2	90.2	87.4	72.6	60.3	46.5	10.0

[a]Experimental data extrapolated to provide estimates of ionization rates over a wide range of altitudes and geomagnetic cutoffs.

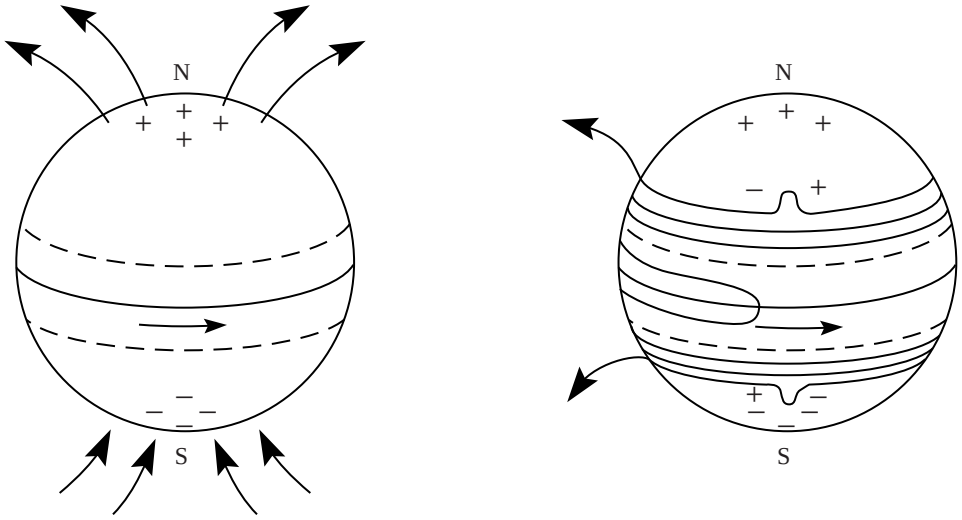

(a) Cycle start. (b) Cycle progression.

Figure 1. The Babcock solar cycle model. (Adapted from Withbroe, ref. 3.)

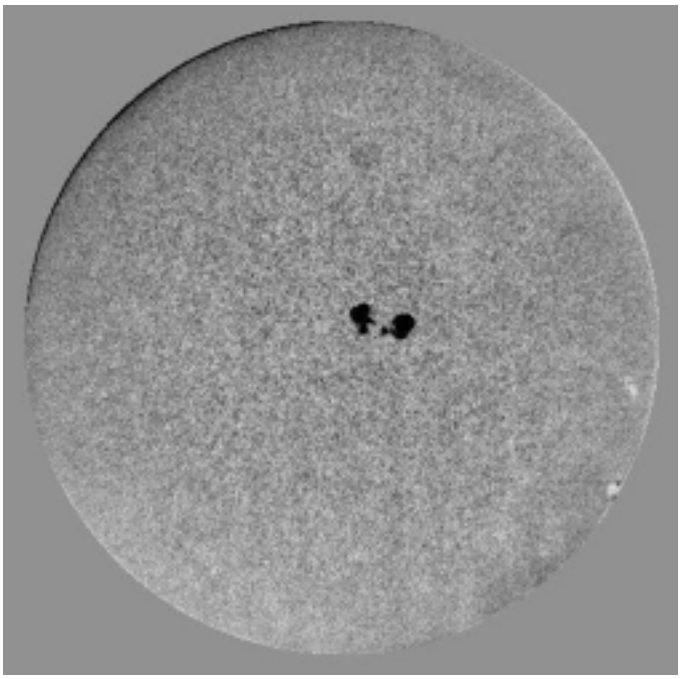

Figure 2. Full-disk white light image of Sun on November 26, 1996, showing sunspots and bright plage region in midst of two spots on lower western limb. (Reprinted with permission of the Big Bear Solar Observatory, www.bbso.njit.edu.)

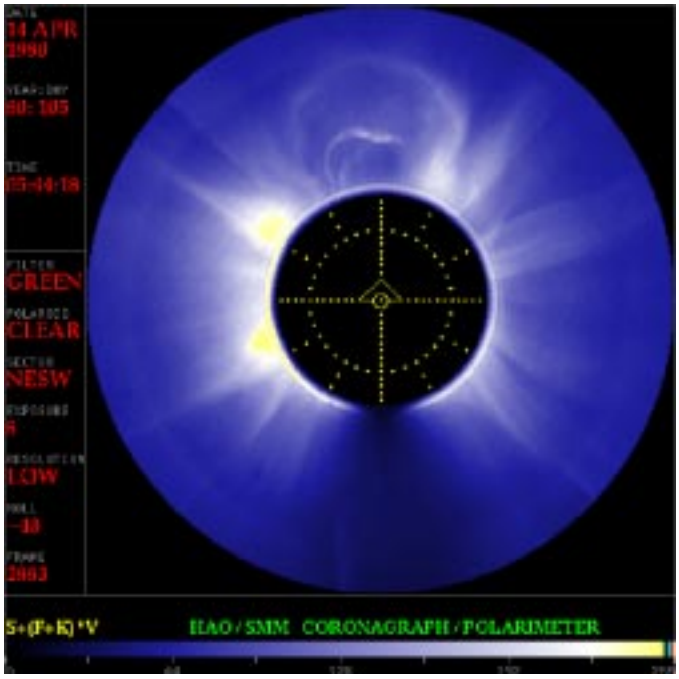

Figure 3. Coronagraph of Sun showing coronal mass ejection near solar maximum on April 14, 1980. (Reprinted with permission of the University Corporation for Atmospheric Research, www.hao.ucar.edu.)

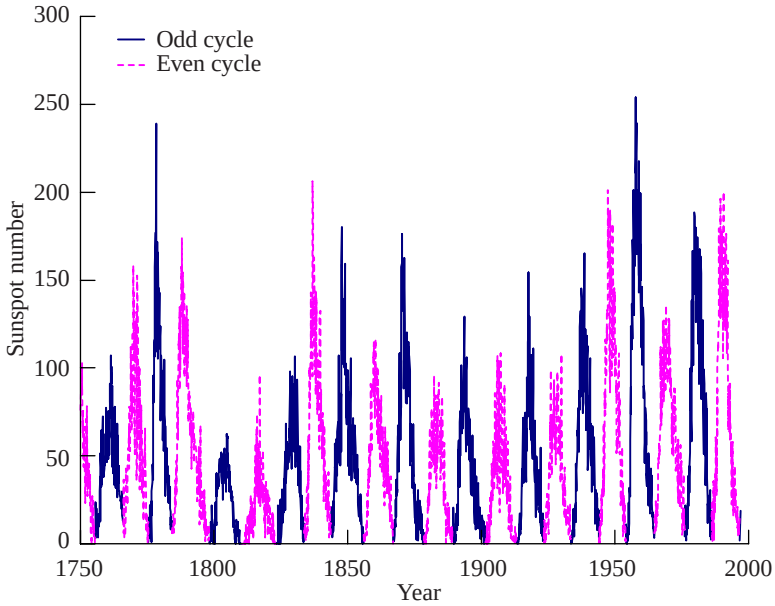

Figure 4. Sunspot number database from 1750 to present. (Data provided by NOAA, www.sec.noaa.gov.)

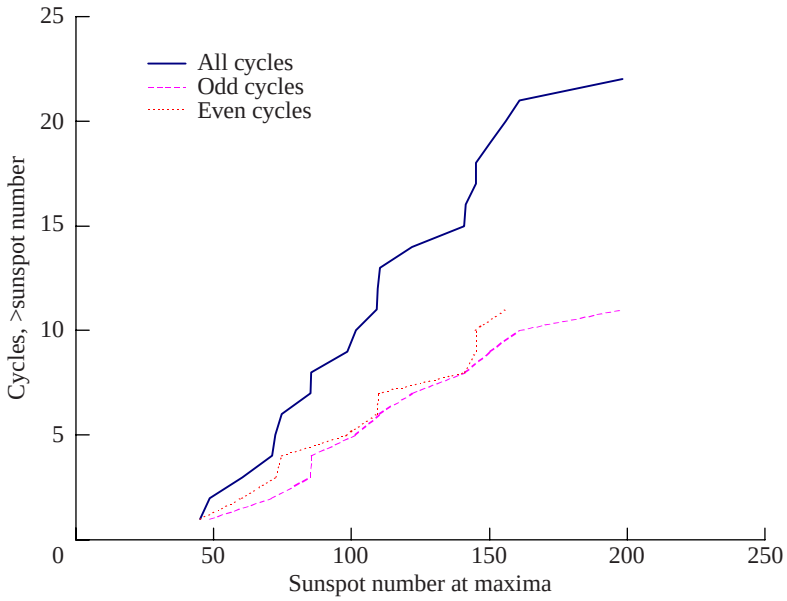

Figure 5. Cumulative frequency distribution of cycle maxima smoothed sunspot number.

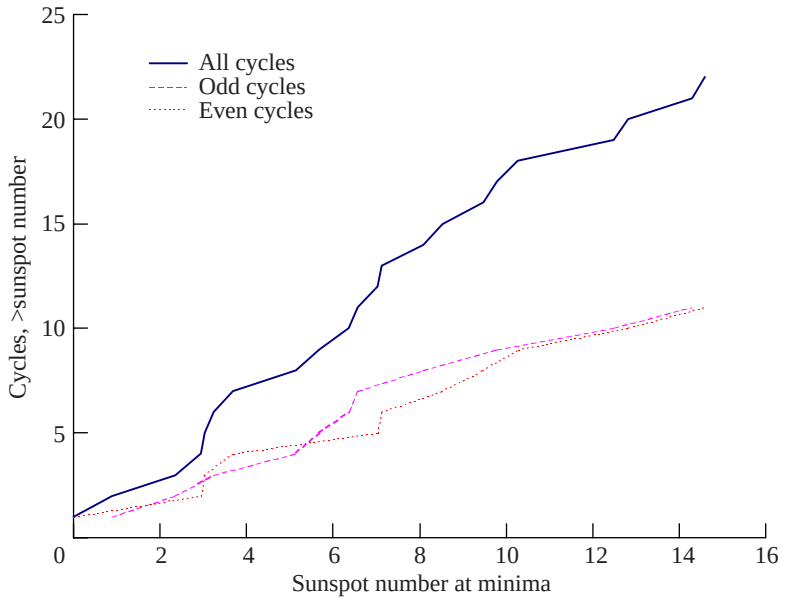

Figure 6. Cumulative frequency distribution of cycle minima smoothed sunspot number.

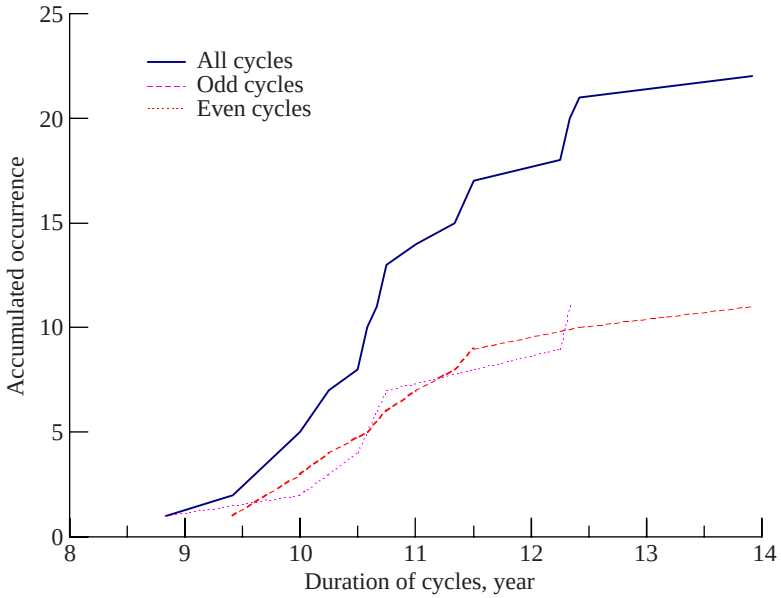

Figure 7. Cumulative frequency distribution of cycle duration.

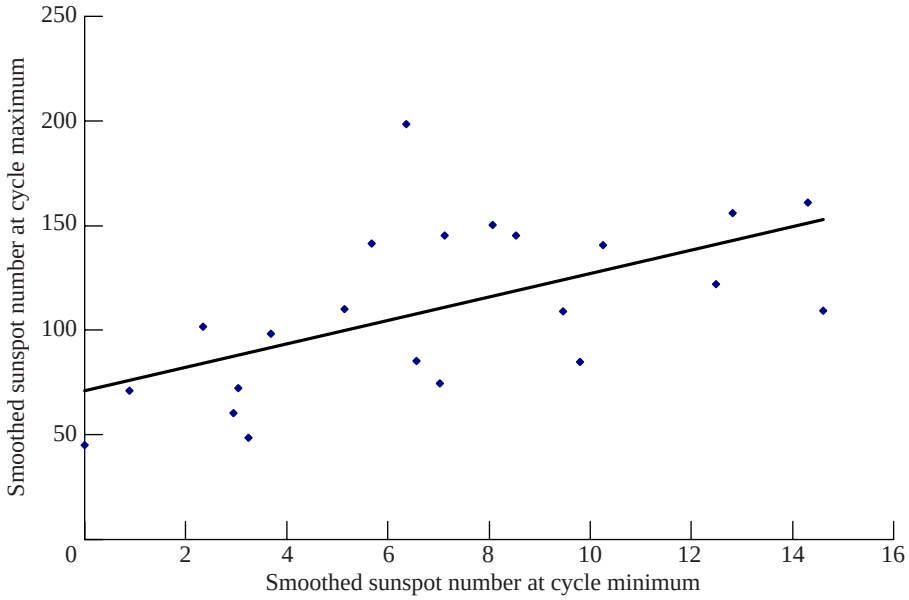

Figure 8. Correlation of smoothed maxima of sunspot cycle with smoothed minimum.

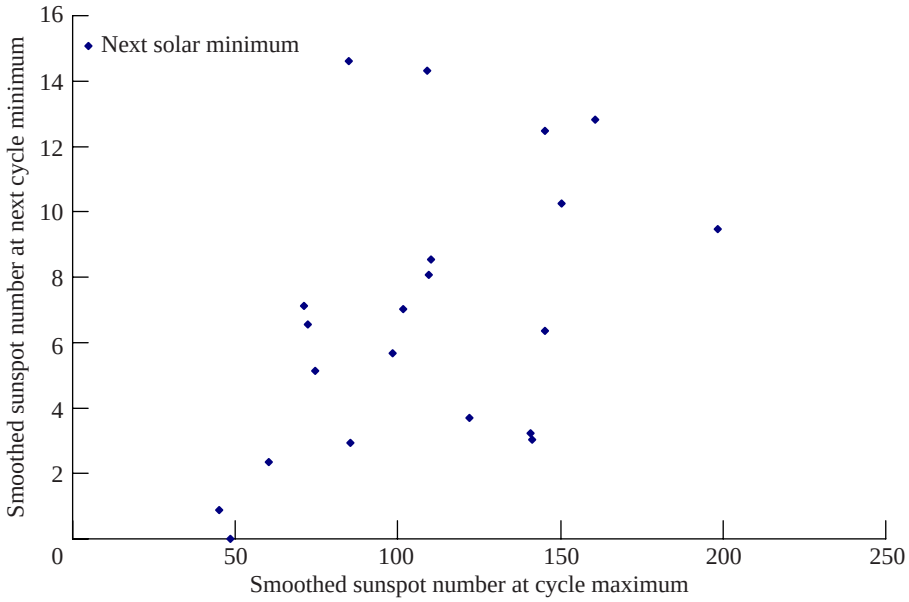

Figure 9. Scatter graph comparing smoothed minima of next cycle, with prior cycle maxima showing no correlation between cycles.

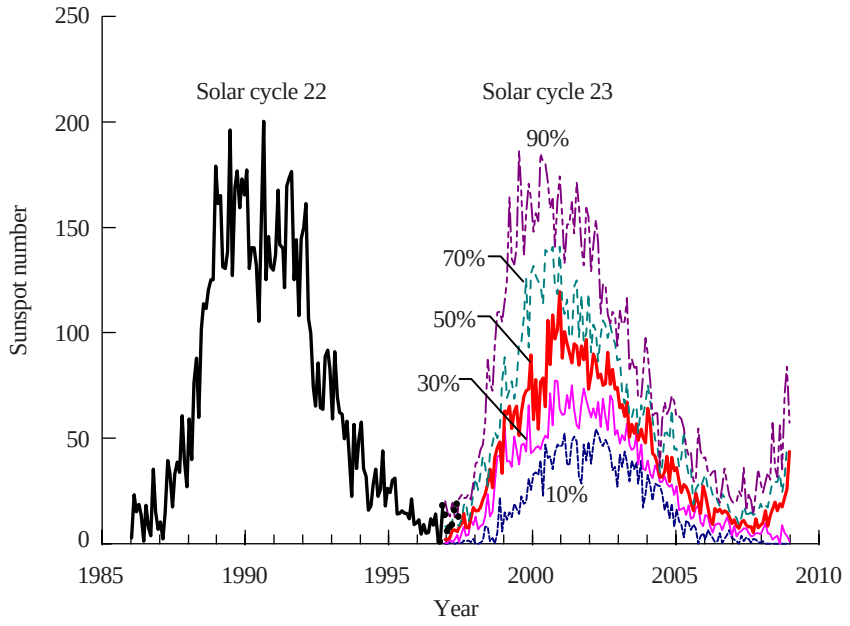

Figure 10. Solar cycle 22 data followed by population distributions of sunspot numbers for all even-numbered cycles. First several monthly averaged sunspot numbers of cycle 23 are shown as data points.

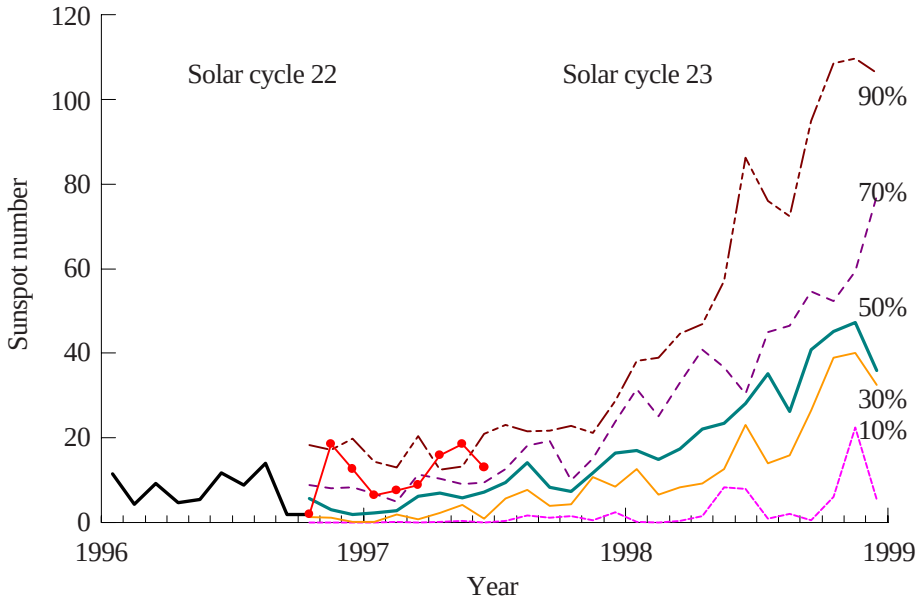

Figure 11. Ending of cycle 22 is taken as September 1996. First 9 months of cycle 23 are used to determine population group of cycle 23.

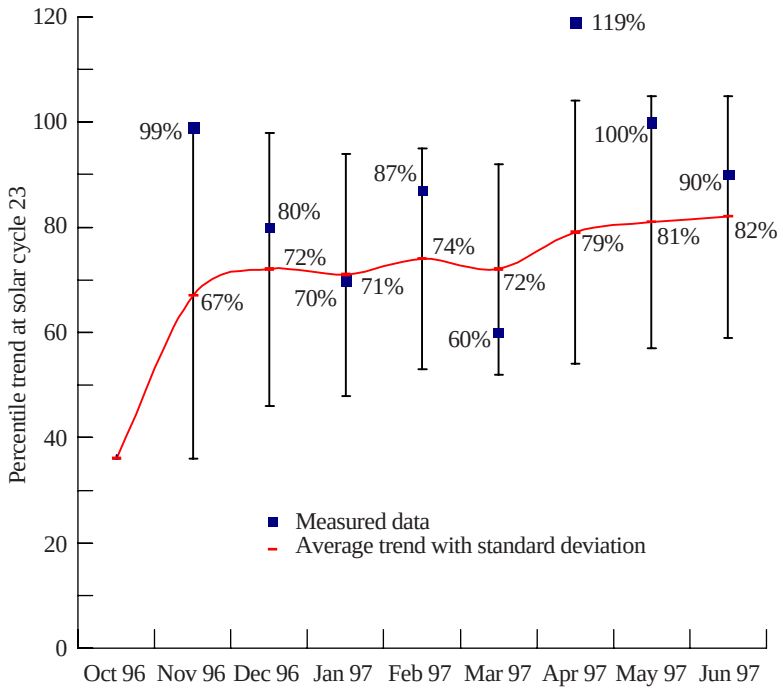

Figure 12. Percentile group of first 9 months of cycle 23 and cumulative mean value and statistical fluctuation.

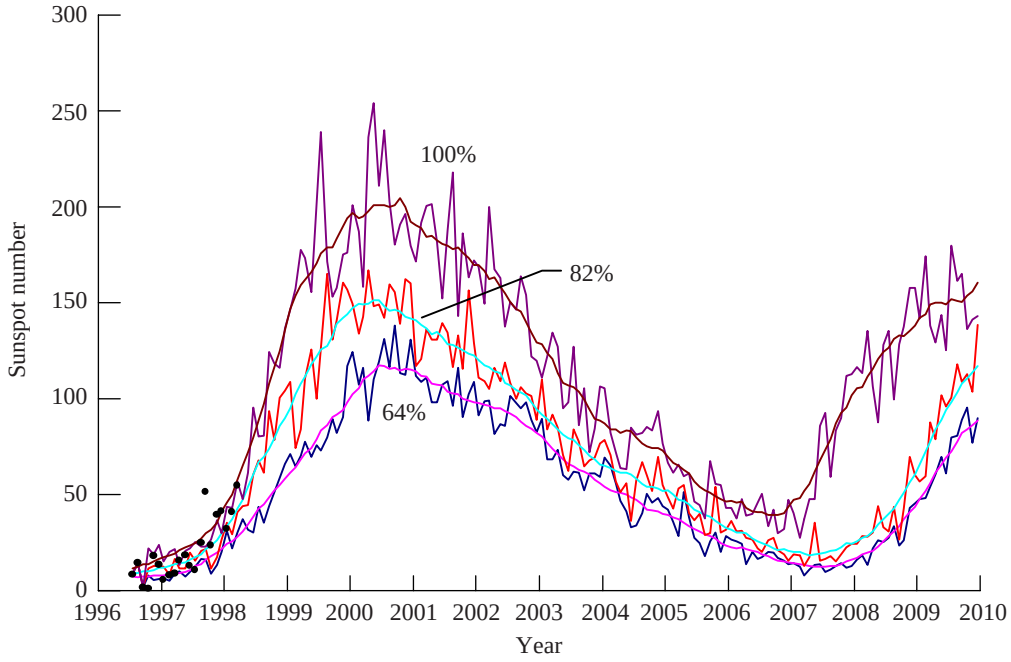

Figure 13. Projected cycle 23 sunspot number and statistical uncertainty. Also shown is new cycle 23 sunspot data since projection was made. (Compare with fig. 11.)

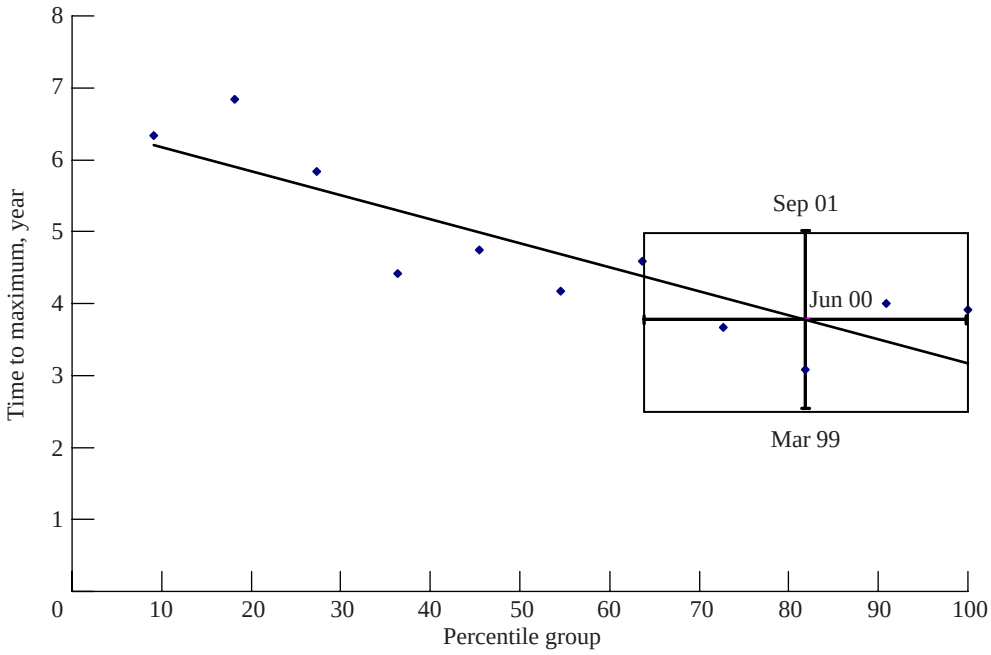

Figure 14. Predicted time to maximum of cycle 23 based on first 9 months of cycle 23 data.

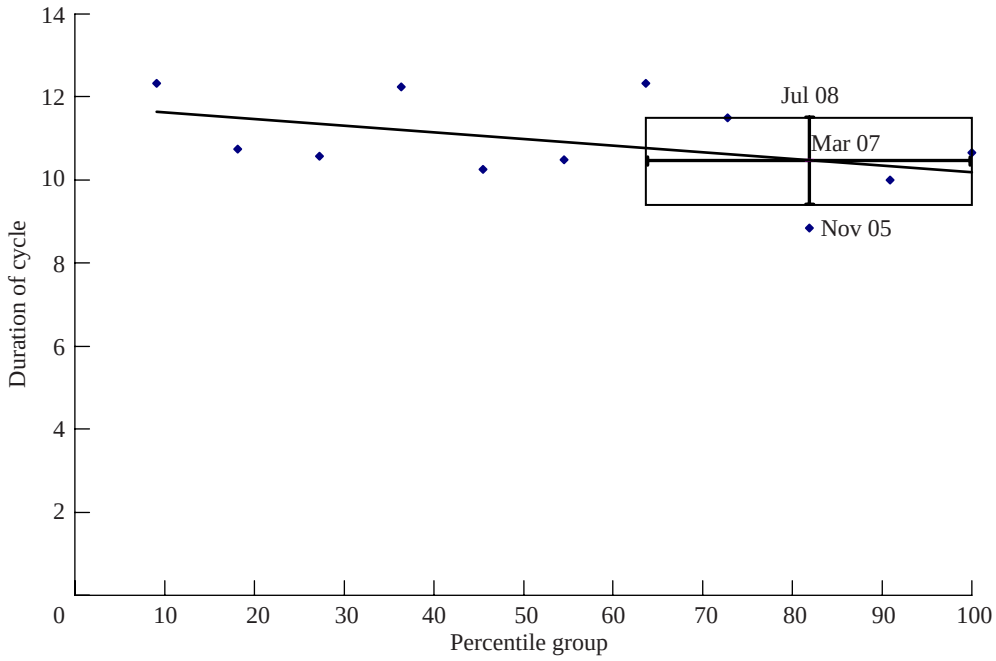

Figure 15. Predicted duration of cycle 23 based on first 9 months of cycle 23.

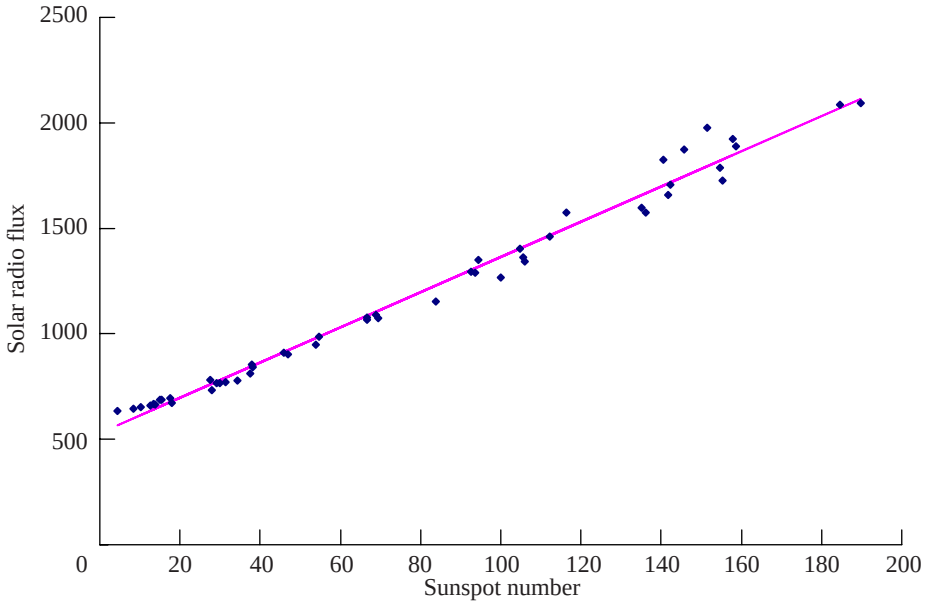

Figure 16. Correlation of solar radio flux W/m^2-s with sunspot number.

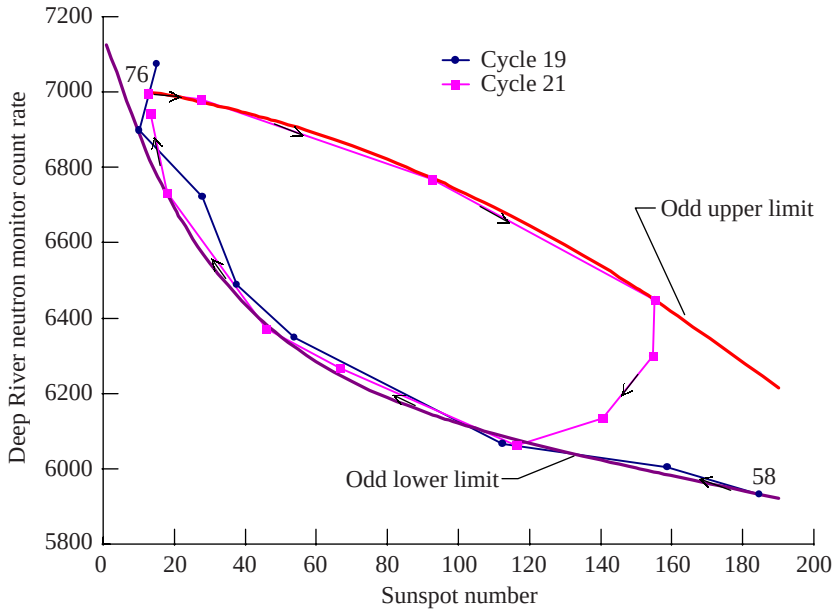

Figure 17. Correlation of Deep River neutron monitor count rate, with sunspot number for cycles 19 and 21.

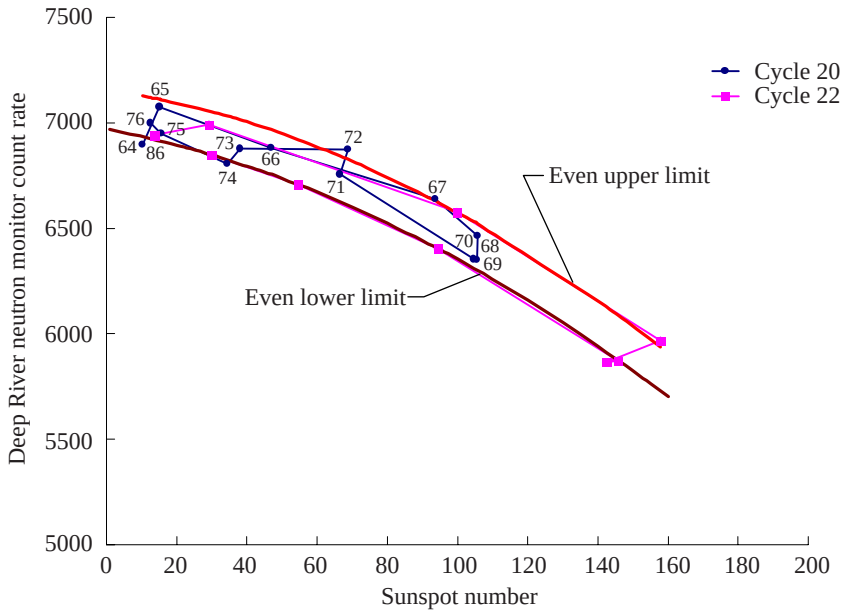

Figure 18. Correlation of solar Deep River neutron monitor count rate, with sunspot number for cycles 20 and 22.

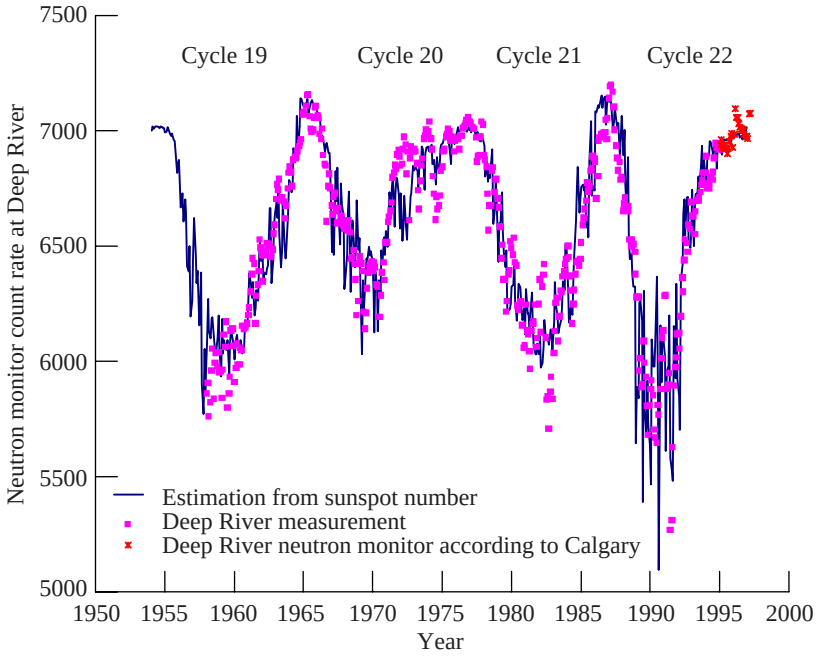

Figure 19. Predicted Deep River neutron monitor count rate using actual sunspot number data and correlation functions in figures 17 and 18 compared with measured data.

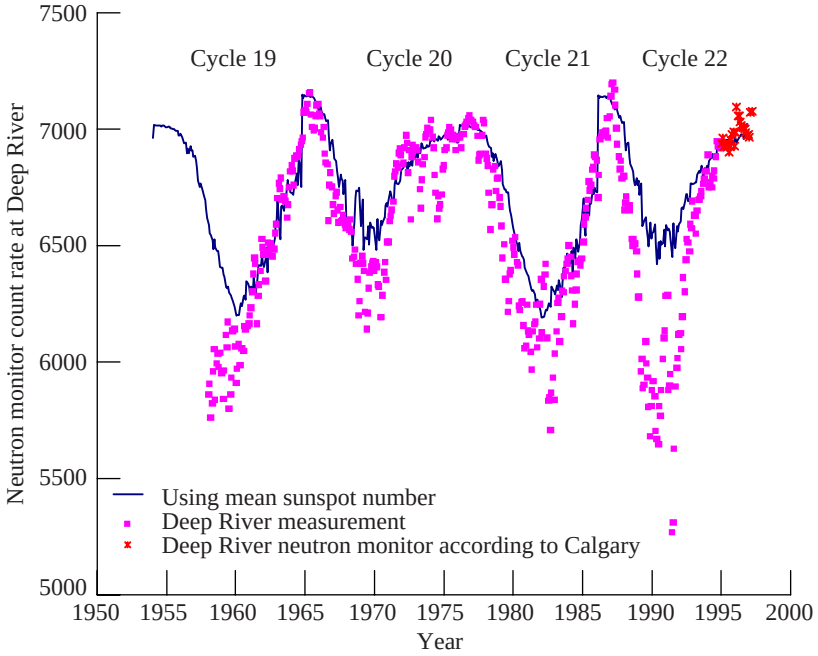

Figure 20. Predicted Deep River neutron monitor count rate using odd and even cycle expectation values compared with measured data.

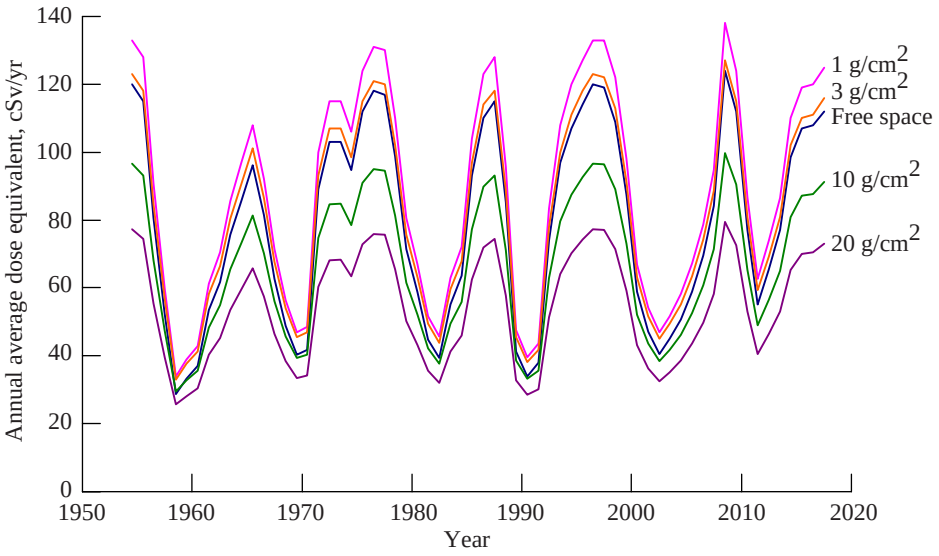

Figure 21. Annual average surface 0-cm depth dose equivalent behind aluminum shield of various thicknesses.

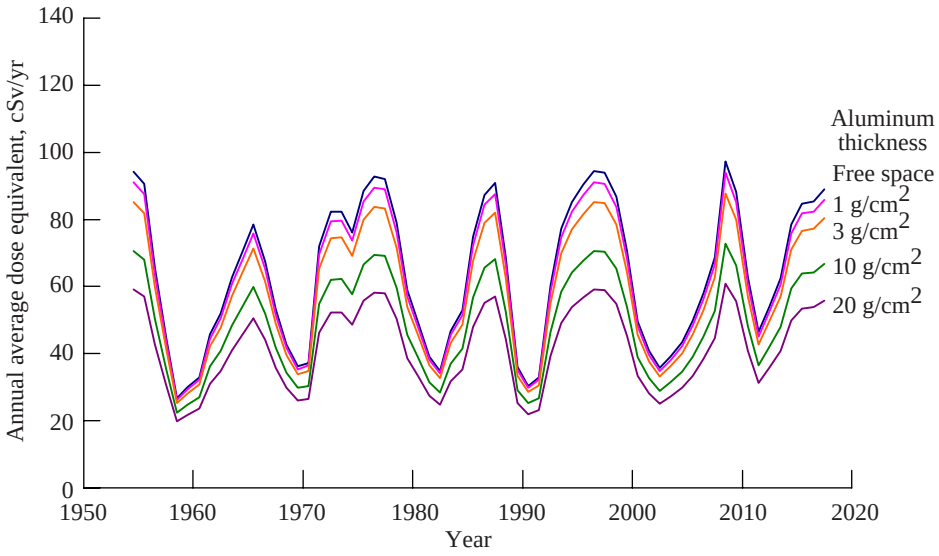

Figure 22. Annual average 5-cm depth dose equivalent behind aluminum shield of various thicknesses.

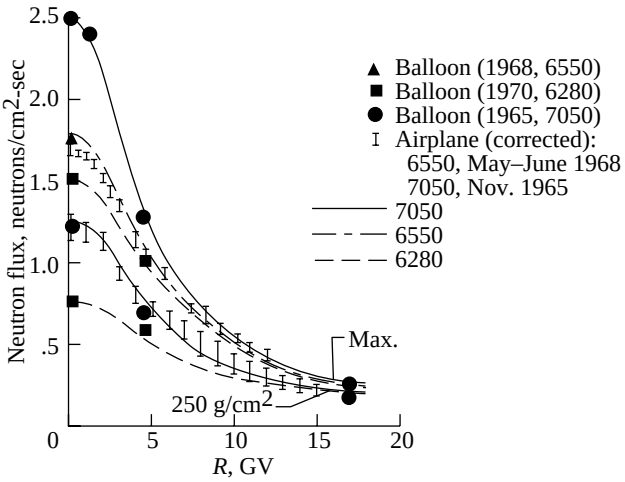

Figure 23. Fast neutron flux (in range of 1 to 10 MeV) at transition maximum and at 250-g/cm^2 depth, as a function of vertical cutoff rigidity *R* for various times in solar cycle and Deep River neutron monitor count rates.

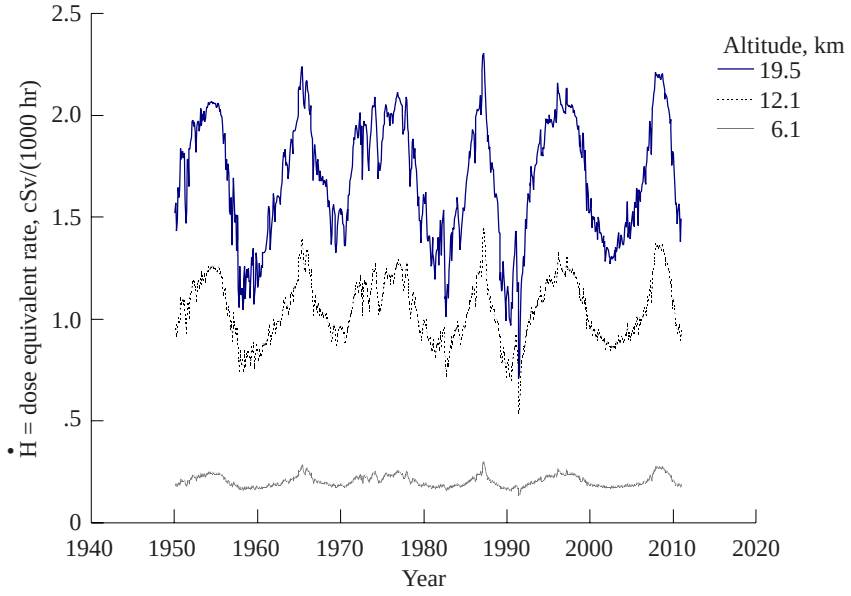

Figure 24. Dose equivalent at three altitudes in atmosphere at high latitudes.

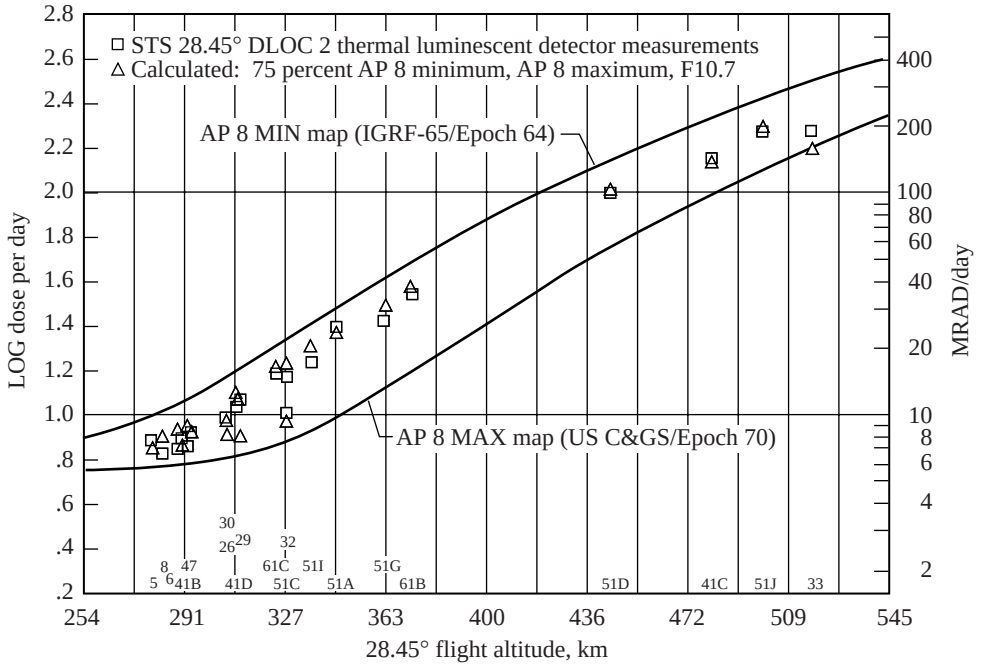

Figure 25. Daily dose for Shuttle in 28.5° orbit at various stages of solar cycle and altitude. Triangles are calculations interpolated according to F10.7 at time of flight. (STS is Space Transportation System; DLOC is dosimeter location; GCR is galatic cosmic rays; and USC&GS is United States Coast and Geodetic Survey.)

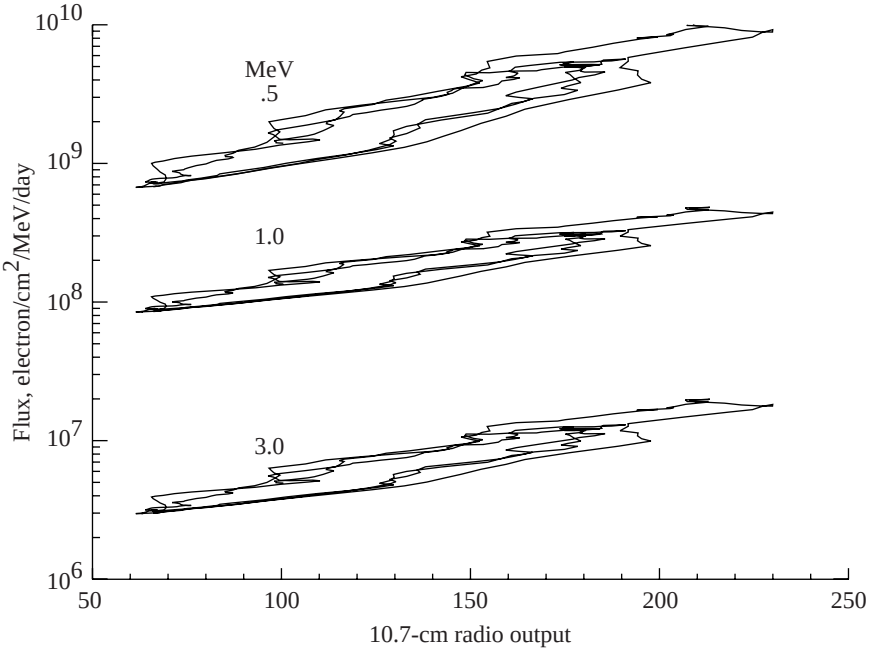

(a) Electron odd cycles.

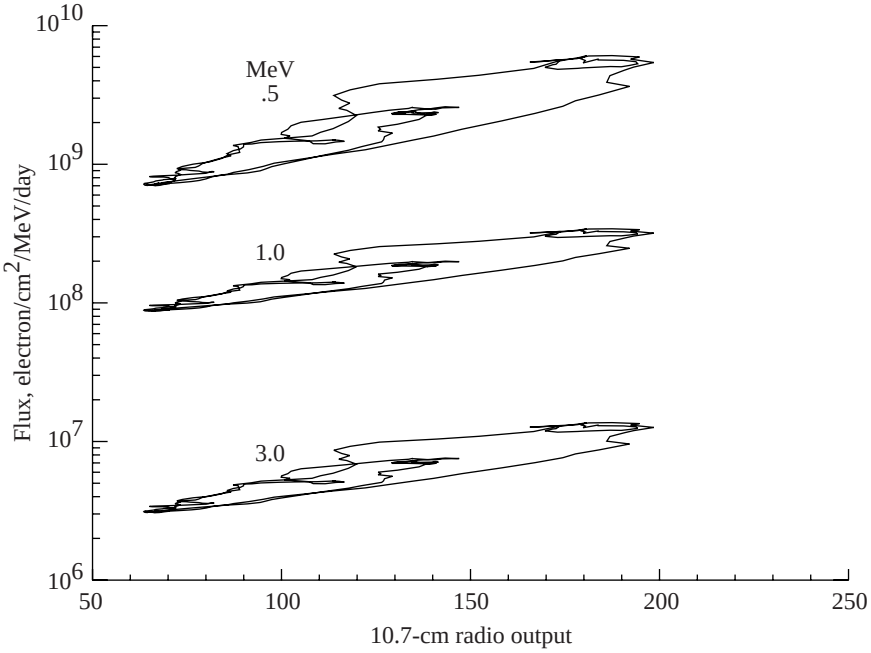

(b) Electron even cycles.

Figure 26. Solar cycle variation of electron flux in 51.6° inclination at 400-km altitude during odd and even cycles for 1955 to 2005.

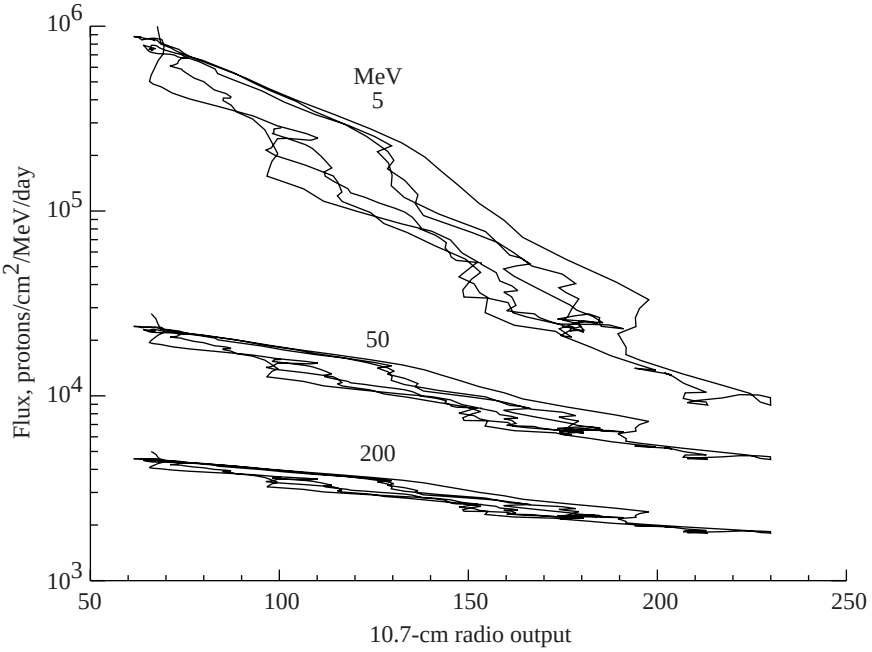

(a) Proton odd cycles.

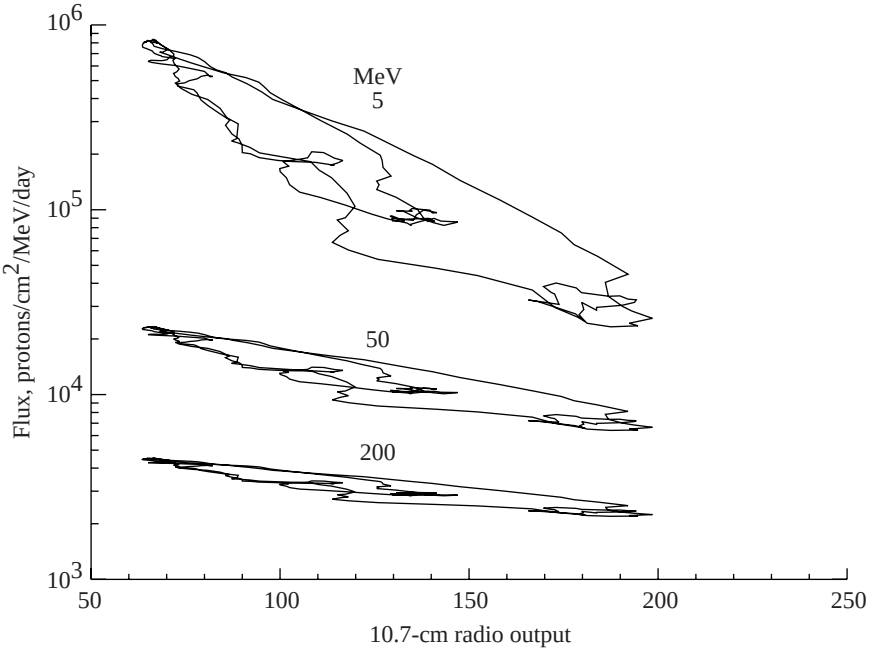

(b) Proton even cycles.

Figure 27. Solar cycle variation of proton flux in 51.6° inclination at 400-km altitude during odd and even cycles for 1955 to 2005.

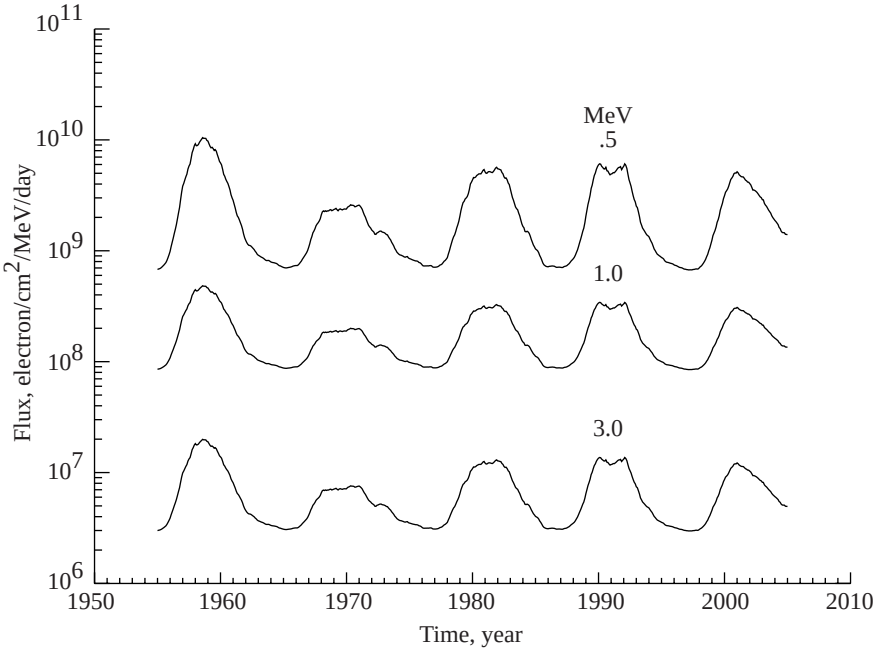

(a) Temporal variation of electronic flux.

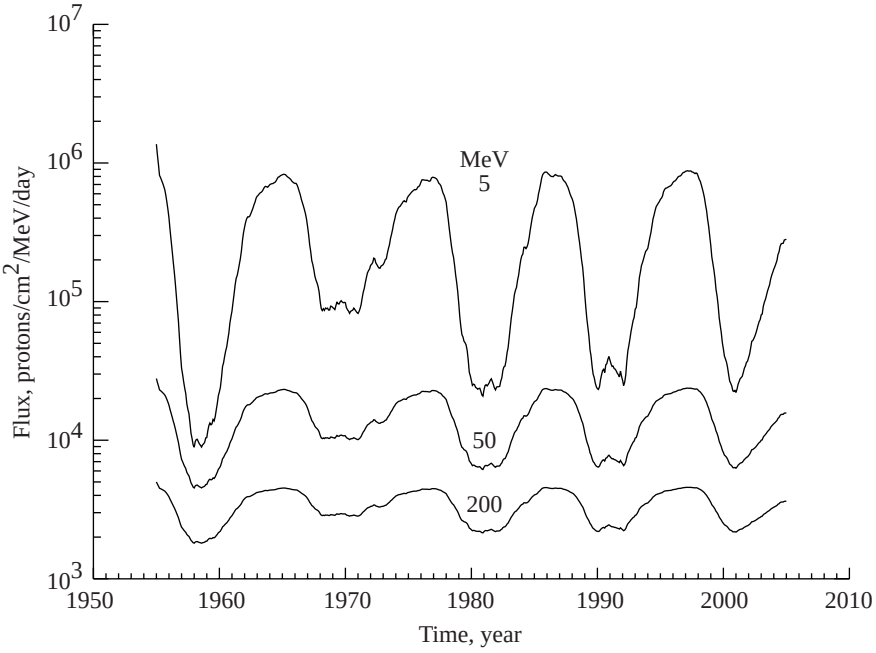

(b) Temporal variation of proton flux.

Figure 28. Time variation of electron flux and proton flux in 51.6° inclination at 400-km altitude for 1955 to 2005.

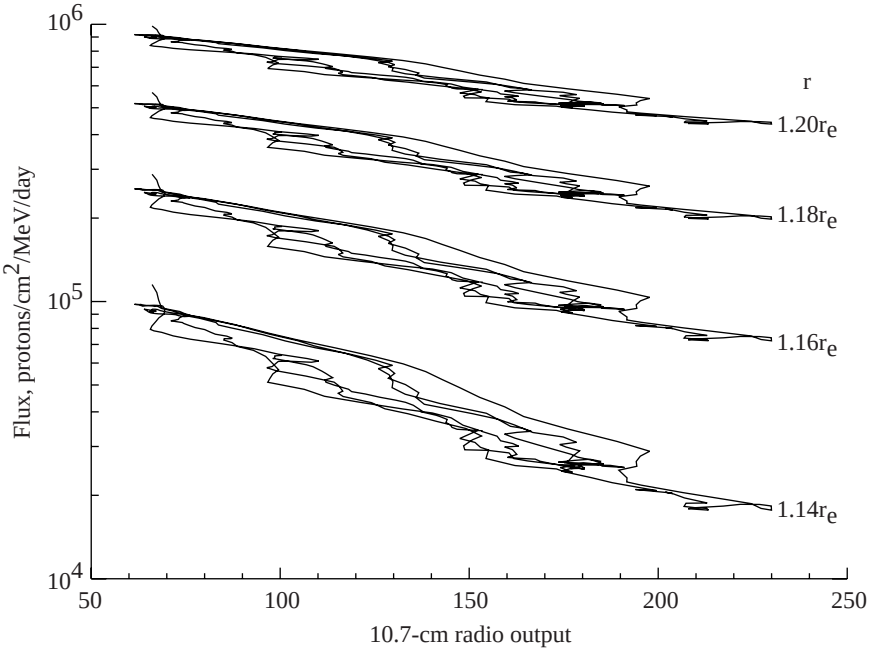

(a) Proton flux for odd cycles at four altitudes.

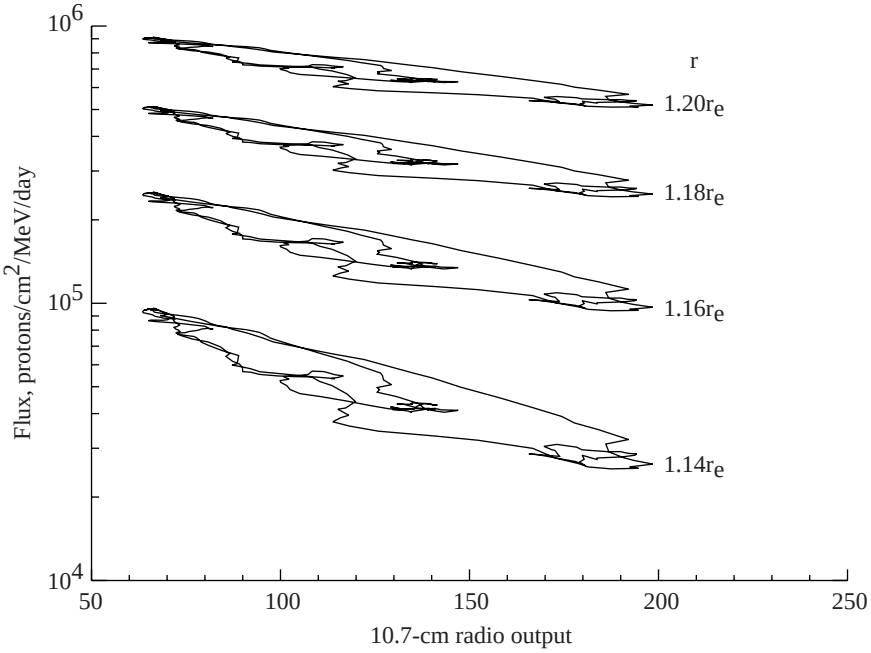

(b) Proton even cycles at four altitudes.

Figure 29. Solar cycle variation of 100 MeV proton flux for odd and even cycles in equatorial orbit at various altitudes. (The symbol r is radial distance; the symbol r_e is radius of the Earth.)

REPORT DOCUMENTATION PAGE

Form Approved
OMB No. 07704-0188

Public reporting burden for this collection of information is estimated to average 1 hour per response, including the time for reviewing instructions, searching existing data sources, gathering and maintaining the data needed, and completing and reviewing the collection of information. Send comments regarding this burden estimate or any other aspect of this collection of information, including suggestions for reducing this burden, to Washington Headquarters Services, Directorate for Information Operations and Reports, 1215 Jefferson Davis Highway, Suite 1204, Arlington, VA 22202-4302, and to the Office of Management and Budget, Paperwork Reduction Project (0704-0188), Washington, DC 20503.

1. AGENCY USE ONLY *(Leave blank)*	2. REPORT DATE	3. REPORT TYPE AND DATES COVERED
	September 1999	Technical Publication

4. TITLE AND SUBTITLE
Solar Cycle Variation and Application to the Space Radiation Environment

5. FUNDING NUMBERS
WU 199-45-16-12

6. AUTHOR(S)
John W. Wilson, Myung-Hee Y. Kim, Judy L. Shinn, Hsiang Tai, Francis A. Cucinotta, Gautam D. Badhwar, Francis F. Badavi, and William Atwell

7. PERFORMING ORGANIZATION NAME(S) AND ADDRESS(ES)
NASA Langley Research Center
Hampton, VA 23681-2199

8. PERFORMING ORGANIZATION REPORT NUMBER
L-17780

9. SPONSORING/MONITORING AGENCY NAME(S) AND ADDRESS(ES)
National Aeronautics and Space Administration
Washington, DC 20546-0001

10. SPONSORING/MONITORING AGENCY REPORT NUMBER
NASA/TP-1999-209369

11. SUPPLEMENTARY NOTES
Wilson, Kim, Shinn, and Tai: Langley Research Center, Hampton, VA; Cucinotta and Badhwar: Johnson Space Center, Houston, TX; Badavi: Christopher Newport University, Newport News, VA; Atwell: Boeing North American, Houston, TX

12a. DISTRIBUTION/AVAILABILITY STATEMENT
Unclassified–Unlimited
Subject Category 92 Distribution: Standard
Availability: NASA CASI (301) 621-0390

12b. DISTRIBUTION CODE

13. ABSTRACT ***(Maximum 200 words)***

The interplanetary plasma and fields are affected by the degree of disturbance that is related to the number and types of sunspots in the solar surface. Sunspot observations were improved with the introduction of the telescope in the seventeenth century, allowing observations which cover many centuries. A single quantity (sunspot number) was defined by Wolf in 1848 that is now known to be well correlated with many space observable quantities and is used herein to represent variations caused in the space radiation environment. The resultant environmental models are intended for future aircraft and space-travel-related exposure estimates.

14. SUBJECT TERMS
Space radiations; Cosmic rays; Atmospheric radiations; Solar cycles

15. NUMBER OF PAGES
36

16. PRICE CODE
A03

17. SECURITY CLASSIFICATION OF REPORT	18. SECURITY CLASSIFICATION OF THIS PAGE	19. SECURITY CLASSIFICATION OF ABSTRACT	20. LIMITATION OF ABSTRACT
Unclassified	Unclassified	Unclassified	UL